

A 10,000 star spectroscopic survey of the thick disk-halo interface : Phase-space sub-structure in the thick disk

Apoorva Jayaraman^{1*}, Gerard Gilmore¹, Rosemary F.G. Wyse², John E. Norris³, Vasily Belokurov¹

¹*Institute of Astronomy, Madingley Rd, Cambridge CB3 0HA, UK*

²*Johns Hopkins University, Department of Physics and Astronomy, 3900 North Charles Street, Baltimore, MD 21218, USA*

³*Research School of Astronomy and Astrophysics, Australian National University, Mount Stromlo Observatory, Cotter Road, Weston, ACT 2611, Australia*

Accepted 2013 February 4. Received 2013 February 4; in original form 2012 October 6

ABSTRACT

We analyse a 10,000 star spectroscopic survey, focused on Galactic thick disk stars typically 2-5 kpc from the Sun, carried out using the AAOmega Spectrograph on the AAT. We develop methods for completeness-correction of the survey based on SDSS photometry, and we derive star distances using an improved isochrone-fitting method with accuracies better than 10%. We determine the large-scale kinematic ($V_\phi=172$ km/s and $\sigma(\phi, r, z) = (49, 51, 40)$ km/s.), and abundance properties of the thick disk, showing these representative values are a fair description within about 3 kpc of the sun, and in the range 1-3 kpc from the Galactic Plane. We identify a substantial overdensity in lines of sight towards the inner Galaxy, with metallicity $[\text{Fe}/\text{H}] \sim -1$ dex, and higher line of sight velocities than the thick disk, localised along the direction $(\ell, b) = (48^\circ, -26^\circ)$. This overdensity appears to be towards, but closer than, the known Hercules-Aquila halo overdensity and may be related to the Humphreys-Larsen inner galaxy thick disk asymmetry.

Key words: Galaxy: kinematics and dynamics; Galaxy: stellar content; surveys; Galaxy: abundances

1 INTRODUCTION

The advent of large-area photometric and spectroscopic surveys in the recent decade has made observational studies of the Galactic stellar populations extremely vibrant. Rapid progress is being made in obtaining independent descriptions of the chemical, kinematic and spatial distributions, especially of the thick disk and halo, although systematic challenges remain associated particularly with the definitions of stellar populations. Photometric definitions, which led to discovery of the thick disk, are reviewed by, for example, Gilmore et al. (1989) and the history of such studies up to the present is described by Yoshii (2013). Much recent focus has been on chemical abundance definitions. Those studies based on either small numbers of high quality spectra or large numbers of lower resolution spectra, have become a major industry. They have established that the thick disk is a discrete stellar population, at least in the solar neighbourhood (but *cf.* Bovy et al. (2012) for an orthogonal view), but raised many open questions and incon-

sistent results on gradients, origins, and so on (Fuhrmann (2004, 2008, 2011), Fuhrmann et al. (2012), Reddy (2010, 2007), Reddy & Lambert (2008), Reddy et al. (2008, 2006), Bensby & Feltzing (2012a,b), Bensby et al. (2011, 2012), Lee et al. (2011), Schlesinger et al. (2011), Cheng et al. (2012a,b), Liu & van de Ven (2012), Ruchti et al. (2011)). As just two more of these very many recent examples, Juric et al. (2008) determined the exponential scale height and scale length of the thick disk from Sloan Digital Sky Survey (SDSS) photometric data to be 0.9 kpc and 3.6 kpc respectively. Carollo et al. (2010) re-visited the kinematics of the thick disk and halo using SDSS Data Release 7 (DR7) and particularly investigated the overlaps between known stellar populations to conclude that the metal weak thick disk is a kinematically and chemically distinct component between the halo and thick disk. The main challenge for these kinds of studies has been the intrinsic overlap of population distribution functions, and the associated complexities in how to deconvolve them correctly. Improving constraints then requires a moderately high surface density spectroscopic survey, with accurate photometric and proper motion data, sampling a sufficient range of Galactic coor-

* E-mail: aj@ast.cam.ac.uk

ordinates to support statistical separation of the populations. Much is being learnt, but much remains to be earned, especially from spectroscopy outside the Solar neighbourhood (for example, Kordopatis et. al. (2011))

We present here analysis of a 10,000-star spectroscopic survey, with Anglo-Australian Observatory AAOmega spectroscopy complementing SDSS photometry, that has the potential for single-population and correlated population-overlap studies of the kinematics, chemistry and spatial distribution of the thick disk. This survey uses F/G stars to probe significant distances from the Sun; the chemical abundances of these stars provide information on the enrichment history during early stages of galaxy formation. The radial velocities, along with chemical abundance and spatial distribution, allow us to differentiate between populations. The main scientific objective of this survey was to determine the unbiased distribution functions over kinematics, metallicity and spatial distributions of the thick disk and halo, with emphasis on the region of overlap between these two populations.

In section 2 of this paper we present the data, discuss the selection function and compare the photometry and spectroscopy to SDSS DR7. In section 3 we present a weighting method for completeness correction, and thereafter explain an isochrone fitting technique used to derive distances to the stars. In this same section, we also provide a brief discussion of the proper motions (taken from SDSS DR7) and show that the resulting tangential velocities have inevitable large uncertainties. We hence show that, for this study, it is better to exclude proper motions from the analysis and model the data with parameters derivable from the spectroscopic measurements i.e. line of sight velocities, metallicities and distances. In section 4 we outline our method to implement such modelling by marginalising over unknown parameters. We then derive and present our results for the best-fitting kinematic and photometric model of the thick disk, and analyse and characterise the residuals of this model when applied to the data, searching for - and identifying - significant phase-space substructure.

2 THE DATA

2.1 The Survey

A wide-field spectroscopic survey was carried out by Wyse et al. (2006, 2013, (hereafter WGN)) using the AAOmega Spectrograph on the Anglo Australian Telescope, fed by the 400-fibre 2dF facility, targeting lines of sight in the thick disk-halo interface, each covering a two degree field of view. Spectroscopy was obtained for $\sim 10,000$ stars, drawn from the Sloan Digital Sky Survey (SDSS) photometric catalogue, along 32 lines of sight in the region $133^\circ < \text{RA} < 339^\circ$; $-1^\circ < \text{Dec} < 1^\circ$ i.e. along the celestial equator. These cover Galactic longitudes between 228° and 67° at intermediate latitudes ($26^\circ < |b| < 63^\circ$). Table 1 provides the coordinates of all the observed lines of sight along with the number of stars analysed in each field.

Iron abundances were derived from medium resolution spectra ($R=6000$) covering 3700\AA to 4700\AA using a methodology based originally on that developed by Beers et al. (1999) and extended by WGN. The technique,

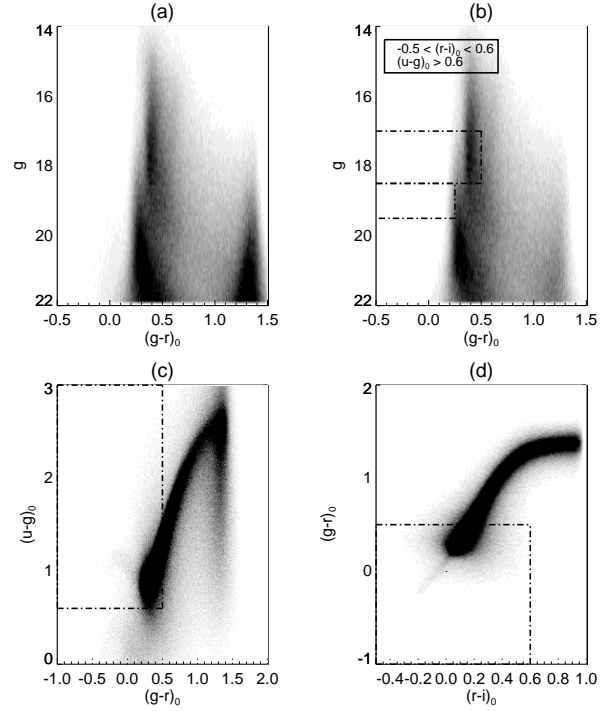


Figure 1. The WGN selection function to isolate stars from the thick disk-halo interface (Wyse et al. 2013) [a] colour-magnitude diagram of data from SDSS DR7 covering 32 fields spanning $-1^\circ < \text{Dec} < 1^\circ$ and $133^\circ < \text{RA} < 339^\circ$, and a broad selection function : $14 \leq g_0 \leq 22$, $-1 \leq (g-r)_0 \leq 1.7$, $-1 \leq (r-i)_0 \leq 1$, $(u-g)_0 \geq 0$. The main Galactic stellar populations seen in this CMD are - the thin disk near $(g-r)_0 \sim 1.3$, the thick disk (brighter) and halo (fainter) near $(g-r)_0 \sim 0.4$; [b] CMD of (a) with the following selection : $-0.5 < (r-i)_0 < 0.6$, $(u-g)_0 \geq 0.6$. This significantly reduces thin disk contamination. The area enclosed within the dot-dashed box denotes the region that is selected from g vs $(g-r)_0$ space to isolate stars from the thick disk-halo interface; [c,d] Colour-colour diagram for the same data as in (a). The $(u-g)_0$ cut mainly eliminates quasars while the $(g-r)_0$ and $(r-i)_0$ cuts eliminate thin disk and binary stars. The dot-dashed box again indicates the selected region of thick disk-halo interface stars isolated for study here.

which uses the CaK-line to determine iron abundance, is calibrated using halo and thick disk field stars. We measured abundances only for spectra having more than 100 net counts per 0.34\AA pixel at 4150\AA . The typical median counts for the sample is 250 per 0.34\AA pixel at 4150\AA . As noted below, this leads to an abundance uncertainty of $\Delta[\text{Fe}/\text{H}] \sim 0.2$ dex. Radial velocities were determined by cross correlation against sky and standard stars, providing velocities with random plus systematic accuracy better than 10 km/s .

The selection function employed in obtaining the data was as follows:

$$\begin{aligned} 17.0 &< g < 18.5 \\ -1.0 &< (g-r)_0 < 0.5 \\ -0.5 &< (r-i)_0 < 0.6 \\ (u-g)_0 &\geq 0.6 \end{aligned}$$

This selection function preferentially selects thick disk and halo stars, mainly F/G dwarfs, and minimises contamination

Table 1. Fields Covered by the WGN Data

RA,Dec deg	l, b deg	Mean Reddening E(B-V)	Number of Stars analysed from WGN	Number of Stars SDSS DR7	% Completeness of WGN spectra wrt SDSS DR7
133 ,0	228, 27	0.033	288	2907	10
135 ,0	229, 28	0.035	236	2523	9
139 ,0	231, 32	0.030	254	1855	13
141 ,0	233, 33	0.032	26	1713	1
145 ,0	235, 37	0.064	268	1524	17
153 ,0	242, 43	0.036	255	1280	20
159 ,0	247, 48	0.065	304	1210	25
161 ,0	249, 49	0.047	299	1238	24
163 ,0	251, 50	0.046	130	1211	10
175 ,0	268, 58	0.021	134	1187	11
179 ,0	275, 60	0.022	118	1255	9
185 ,0	286, 62	0.024	262	1242	21
189 ,0	295, 63	0.021	123	1376	9
197 ,0	312, 63	0.023	294	1559	19
199 ,0	316, 62	0.028	253	1546	16
203 ,0	324, 61	0.027	274	1717	16
205 ,0	328, 60	0.028	257	1790	14
213 ,0	341, 57	0.041	199	2190	9
217 ,0	347, 54	0.039	270	2428	11
223 ,0	354, 50	0.047	288	2836	10
229 ,0	1, 45	0.057	574	2669	15
235 ,0	6, 41	0.100	209	4668	5
237 ,0	7, 39	0.093	275	4859	5
239 ,0	9, 38	0.113	447	4401	10
249 ,0	16, 29	0.107	600	6150	10
313 ,0	48, -26	0.096	756	10754	7
315 ,0	49, -28	0.081	498	9101	5
317 ,0	50, -30	0.097	235	7614	3
319 ,0	51, -31	0.081	527	6410	8
323 ,0	54, -35	0.048	194	4732	4
333 ,0	62, -43	0.069	264	2477	10
339 ,0	67, -47	0.063	273	1680	16

from the thin disk population. In addition, in several fields, fainter halo turnoff candidate stars were targeted to exploit periods of very good seeing, together with Blue Horizontal Branch stars. This extra selection was

$$18.5 < g < 19.5$$

$$(g - r)_0 < 0.25$$

although in practise few stars in this faint extension delivered spectra of sufficient signal-to-noise ratio to deliver abundances, and essentially none with $g > 19.0$.

Figure 1(a) shows the colour-magnitude diagram (CMD) for all stars in the region $133^\circ < \text{RA} < 339^\circ$ and $-1^\circ < \text{Dec} < 1^\circ$ from the SDSS Data Release 7 (Abazajian et al. 2009). The group of stars centred around $(g-r)_0 = 1.3$ and faint apparent magnitudes are intrinsically faint, nearby, low mass stars. These, from their kinematics and metallicity estimates, are identified to be thin disk stars. The stars centred around $(g-r)_0 = 0.4$ are older populations of stars with a bluer main sequence turn-off. There is a shift at about $g_0 = 18.5$ in the average colour of the stars, and this is caused due to the different metallicities of the two groups of stars. The stars with brighter apparent magnitudes have a relatively redder turn off, due to relatively higher metallicity - this is the thick disk population. The stars with bluer turn-off have comparably old ages, but

lower metallicity compared to the thick disk, and are halo stars.

Figure 1(b) illustrates how the CMD changes when the $(r-i)_0$ and $(u-g)_0$ colour cuts are imposed on 1(a). The number of stars is reduced to 75% of the original sample. The $(r-i)_0$ colour-cut preferentially picks out the thick disk and halo stars, over the thin disk ones, while the $(u-g)_0$ colour cut eliminates most quasars. This fact is well illustrated by the colour-colour diagrams in Figure 1(c) and (d). The black squares in 1(b) mark out the g and $(g-r)_0$ colour cuts imposed in this WGN AAOmega Survey. This clearly shows that the selection function achieved the goal of preferentially identifying thick disk and halo stars, while minimising contamination from the thin disk and quasars. The F/G dwarfs thus selected are at distances of a few kpc.

Data Release 4 (DR4) of SDSS served as the original input catalog to the AAOmega Survey. Thus the astrometric and photometric information of the WGN selection function is from SDSS DR4. For this work, the photometry was updated to the more recent Data Release 7 (SDSS DR7).

The stars were cross-matched between DR4 and DR7 based on their unique SDSS identifier. Astrometry and photometry compare well between SDSS DR7 and DR4. The positions of stars from the two datasets are consistent, as expected. The extinction corrected apparent magnitudes

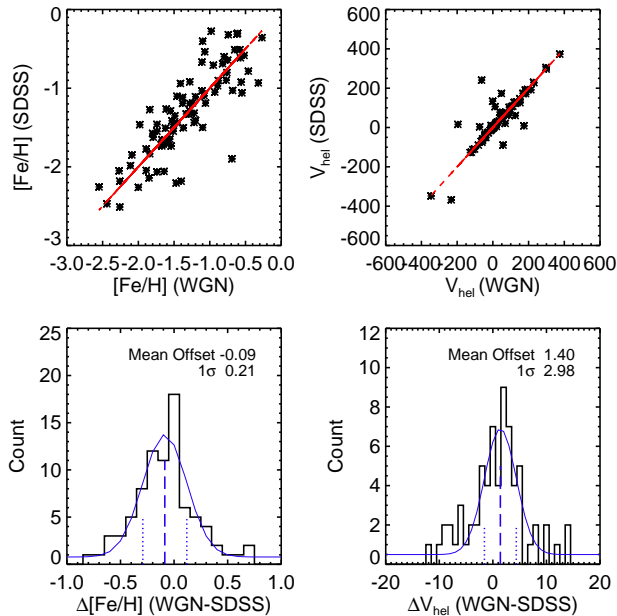


Figure 2. Comparison of derived quantities from Spectroscopy from WGN (AAOmega Survey) to the cross-matched spectroscopy from SDSS DR7. 84 matches are found based on the position of stars. The top 2 panels show scatter plots of $[\text{Fe}/\text{H}]$ and radial velocity from WGN against the values from SDSS DR7, where the dashed line indicates the one-to-one correlation for WGN data. The bottom panels show the distribution of the difference between the two measurements. The black histogram denotes the difference between WGN and SDSS DR7, the blue smooth line shows a gaussian fit to this histogram. The dashed vertical line in each case marks the mean offset of SDSS DR7 spectroscopy from WGN, while the dotted vertical lines marks the 1σ limits of the scatter. The value of the mean offset and 1σ limits for both $[\text{Fe}/\text{H}]$ and radial velocity is indicated in the respective plots.

from DR4 are displaced from the corresponding values from SDSS DR7 by 0.002 magnitude with a 1σ spread of 0.01 magnitude, which is negligible. Similarly so for the $g - r$ colour. This suggests that the recalibration of photometry/extinction effects in DR7 as compared to DR4 is minimal.

Figure 2 shows the comparison between the spectroscopic results of WGN (obtained from measurements in the AAOmega survey) for the 84 stars in common with the spectroscopic observations released as part of SDSS DR7. Metallicity values between the two surveys are in very good agreement: they are offset in the mean by less than about 0.1 dex and show a scatter of 0.2 dex at the 1σ level. Radial velocities from the two surveys are also in good agreement, with a mean offset less than 2 km/s ($1\sigma = 3$ km/s). (The few large outliers are likely to be due to variable stars). Both the metallicity and velocity offsets indicate uncertainties we will adopt for the AAOmega survey.

We thus have available for analysis 32 fields spanning the equatorial stripe, each some 2 degree squared area, centred on the listed line of sight coordinates, with $[\text{Fe}/\text{H}]$ and radial velocities from WGN and *ugriz* photometry and positions from SDSS DR7.

Figure 3 presents an overview of the spectroscopic mea-

surements from the WGN survey. It shows a plot of the measured heliocentric velocity and metallicity vs RA. This broadly indicates the presence of both the non-rotating, metal-poor halo component and the rotating and relatively metal-rich thick disk component. An azimuthal velocity of 180 km/s at a distance of 2 kpc projected onto the line of sight is over-plotted for reference.

3 PROPERTIES AND CALIBRATION OF THE WGN SAMPLE

3.1 Completeness Correction

Completeness is always a significant issue with any spectroscopic dataset as there are many more stars which are present in a given direction of the sky than the number for which we have spectra. With the introduction of multi-fibre spectrographs in the last decade, spectra of multiple objects are now obtained simultaneously but this is still restricted to a few hundred objects per field of view.

There is a further bias towards brighter stars which arises from discarding those spectra from the sample which have low signal-to-noise ratio. The sample for which spectrometric parameters are derivable has an additional bias against metal-poor, hot, blue stars, which generates biased completeness in the purely photometric input selection function, described in Section 2.1.

3.1.1 Completeness of SDSS DR7

We first check the completeness of SDSS by comparing to a deeper dataset, namely COMBO-17. COMBO-17 is a spectrophotometric survey which imaged 5 fields at high Galactic latitudes covering 1 square degree of the sky in 17 optical filters. It obtained deep and sharp r-band data and the selection of stars is complete down to $r \sim 23$ (Wolf et al. 2004).

The SDSS DR7 photometry is sufficiently close to 100% complete in the magnitude range $16.0 < r < 21.0$ (which encompasses the range of the WGN dataset $16.5 < r < 19.0$), in comparison to overlapping fields in the COMBO-17 survey.¹

It is thus reasonable to adopt SDSS DR7 as complete in the magnitude range of relevance to WGN. We therefore go on to use SDSS DR7 to evaluate the completeness of the WGN sample.

3.1.2 Completeness of WGN

We find that the WGN dataset has completeness levels that are as high as 25% of all potential candidates having spectra of sufficient quality to allow derivation of both $[\text{Fe}/\text{H}]$ and radial velocity. The last 2 columns of Table 1 show the number of stars in the given field in the SDSS master photometric catalog (employing the same selection functions as in the data) and the relative completeness of the WGN data field-by-field.

¹ For the comparison of completeness between SDSS and COMBO-17 see http://www.sdss3.org/dr8/imaging/other_info.php

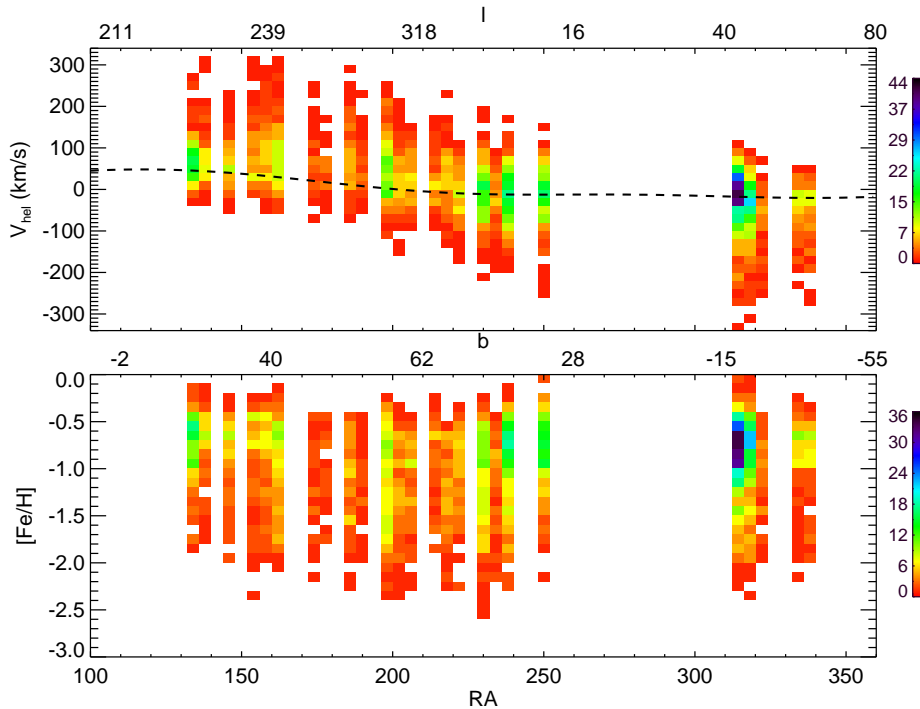


Figure 3. Measured heliocentric velocity and metallicity as a function of RA from the WGN dataset analysed here. The corresponding Galactic longitude l and latitude b of the fields is shown in parallel axes. RA, l and b are quoted in degrees. The colours indicate the number of stars within each pixel (colour-coded in the colour bar) going from red for small to blue for large star count. The black dashed line shows an azimuthal velocity of 180 km/s at a distance of 2 kpc projected onto the line of sight and is over-plotted to guide the eye along the thick disk population.

3.1.3 Weighting Method

We describe here a weighting method in colour-magnitude space to correct the WGN spectroscopic sample for completeness inside the WGN selection function. This method is widely applied in sampling, in situations as diverse as opinion polling and ornithology. We note its applications in studies of the thick disk in astronomy below.

Stars in a colour-magnitude bin of the spectroscopic data are weighted up to the actual number of stars available for observation in that bin, by a weighting factor W which is obtained by taking the ratio of the density function of stars in colour magnitude space $D[g_0, (g-r)_0]$ of the SDSS DR7 catalogue to the data themselves:

$$W = \frac{D_{\text{SDSSDR7}}[g_0, (g-r)_0]}{D_{\text{WGN}}[g_0, (g-r)_0]} \quad (1)$$

Three different methods of computing the density function for both the Sloan photometric superset and the WGN dataset were tried : (a) probability density functions were calculated by convolving each data point with a Gaussian kernel function; (b) one dimensional number density distributions (as a function of apparent magnitude) for individual colour bins were determined by simple polynomial fits to 1D apparent magnitude histograms; (c) a two-dimensional histogram (i.e. number of stars as a function of colour-magnitude) was used to represent the distribution of stars in the colour-magnitude plane.

The three methods provide progressively decreasing de-

grees of smoothing ((a)-most smoothing, (c)-least smoothing) across the colour-magnitude plane.

The pixel or bin choices in each of these methods was made so that we sufficiently resolve the main features of interest on the CMD (i.e. the different Galactic stellar populations), while ensuring that the pixels contain sufficient number of stars relative to the noise level. This choice may also be dependent on line-of-sight.

We found that the distribution functions produced by these three methods did not differ significantly, indicating that the particular method chosen to compute the density distributions in colour magnitude space is not crucial. We chose method (c) as the most robust of the three methods for the rest of the analysis. Along with best performance with low number statistics and ease of computation, this method has particular benefits over the other two. Method (a) involves the risk of the smearing of tiny features that may be of importance through over-smoothing, while edge effects introduce problems in the polynomial fitting technique of method (b).

This weighting function was computed field by field, taking into account that extinction varies across the sky and that the form of the CMD also varies as an effect of the different density profiles of the halo and thick disk. The complete photometric sample from SDSS DR7 was selected for the same colour magnitude cuts, but for a larger spatial region (6x6 degrees) centred on each field, to minimise noise. Colour-magnitude bins of size $\Delta g, \Delta(g-r) = 0.7, 0.13$ mag were found to be an appropriate choice for all fields.

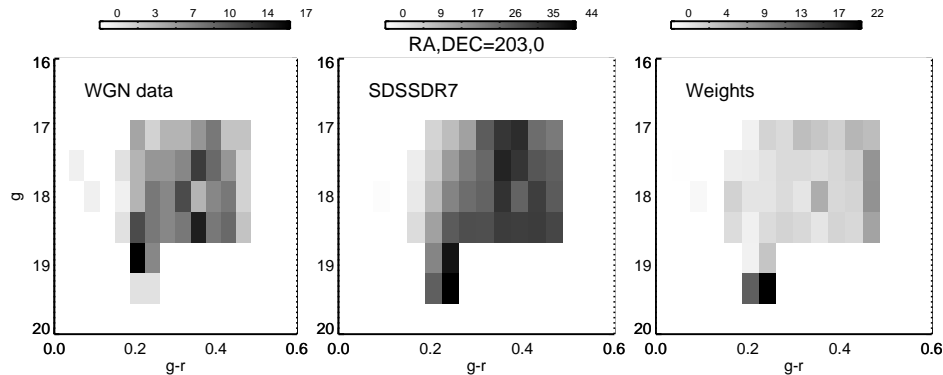


Figure 4. Completeness correction is implemented for the WGN data through a weighting method. This method is illustrated here for the (not untypical) field with coordinates RA, Dec = $203^\circ, 0^\circ$. Left: the distribution in colour magnitude space of the stars observed by WGN in the 2×2 degrees field. Middle: SDSS DR7 data for a 6×6 degrees region centred around the same coordinates, for the same colour-magnitude cuts. Right: the corresponding weights, which are calculated as the ratio of the middle to the left-most panel, multiplied by the area factor, which is given by the area covered on the sky by the left-most panel divided by the area covered by the middle panel

The weighting method is illustrated in Figure 4 for a single field, centred at RA, Dec = $203^\circ, 0^\circ$. The first panel shows the WGN data for a single 2dF field (i.e. a circular field of radius 1 degree centred on the mentioned coordinates). The middle panel shows the SDSS DR7 data for a larger region centred around the same coordinates, for the same colour-magnitude cuts. The last panel shows the weights, which are calculated as the ratio of the counts in the middle to those in the left-most panel, multiplied by an area factor (given by the area covered on the sky by the left-most panel divided by the area covered by the middle panel). In order to avoid large errors from low signal-to-noise pixels, the distribution of weights in every field is cut off at the 90th percentile. Objects having weights greater than the 90th percentile value are reassigned to this new maximum value.

In Figure 5 we illustrate how the metallicity and velocity probability distribution functions (PDF) change when the completeness correction is applied. The histograms shown are for the high-latitude fields, with RA from 190° to 220° . This covers 6 fields at high latitudes ($54^\circ < b < 63^\circ$) in the inner galaxy ($312^\circ < l < 347^\circ$). The data have been split into faint ($g_0 > 18$, top panels) and bright ($g_0 < 18$, bottom panels) stars. In both cases, the unweighted metallicity distributions show a high number of metal-poor stars, particularly in the faint bins, which are likely to be predominantly halo stars given these are high latitude fields. Since we are looking towards the inner galaxy, metal-rich thick disk stars must also be numerous. Applying the weights corrects the distribution for the fact that the data do not show high enough normalisation at the metal-rich end, the effect being more evident in the faint bin. We note that the heliocentric velocity distribution is centred on zero as one would expect for the chosen line-of-sight towards the inner Galaxy. We can see that the velocity distributions are in general smoothed by the completeness correction.

3.1.4 Errors on the Weights

The error on the weight W was calculated as

$$\sigma_w[g_0, (g-r)_0] = \frac{W}{\sqrt{D_{\text{WGN}}[g_0, (g-r)_0]}} \quad (2)$$

Figure 6 shows the cumulative distribution function of percentage errors on the weights. This shows that about 80% of the stars have less than 20% error on their weights. In all further analysis, objects with weight error above 50% were discarded. This eliminated 164 objects from the sample, only 90 of which have $(g-r)_0 > 0.2$ and thus belong to the region of CMD being analysed. Thus by cleaning just 1% of the sample, we remove errant weights without introducing any additional bias to our sample.

3.1.5 Advantages of the adopted weighting method

Weighting the observed data to allow for parameter-dependent incompleteness is a standard requirement in statistical sampling, with many types of approaches. The method we apply here is both very obvious and very simple, and so widely used. To our knowledge it was first applied in determination of the thick disk abundance distribution in section 3.3 of Gilmore et al. (1995), but there may be earlier examples.

In some other investigations (for example, Larsen et al. (2010)), completeness correction is done by comparing the dataset in question with a classical power law, which represents a smooth fit to the number distribution of stars as a function of apparent magnitude, or by comparison to the stellar distribution (in colour-magnitude space) predicted by a Galaxy model, which might also appropriately take into account a model of extinction. The weighting method used here also uses the additional parameter of colour. There is a definite variation of the value of the weights along the colour axis for a given magnitude which makes it important to take into account this additional parameter.

The advantage of this adopted method of accounting for completeness is that it is expected to preserve information from any interesting groups that may exist in velocity-metallicity space, without being limited by potential mismatches between a model and the actual star counts.

Similar methods of completeness correction have been used by some recent papers analysing stars from the Sloan Extension for Galactic Understanding and Exploration survey (SEGUE). Cheng et al. (2012b) employ a sim-

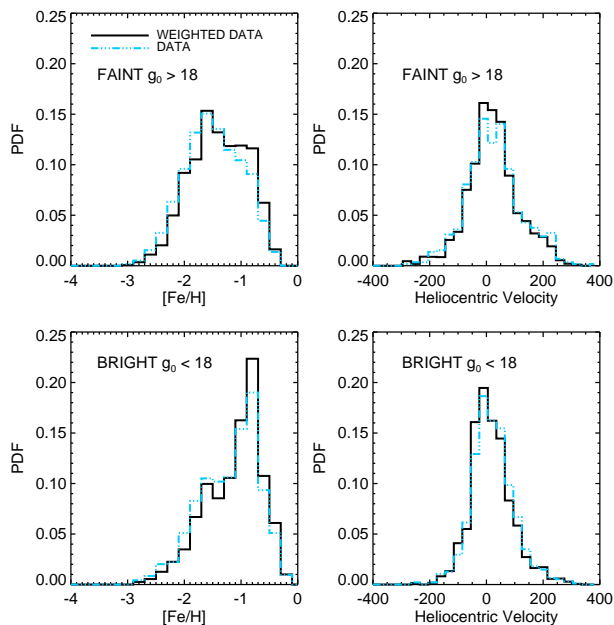


Figure 5. Observed (dashed blue) and Completeness Corrected (solid black) Distribution Functions of $[\text{Fe}/\text{H}]$ and radial velocity for the WGN data fields within $190^\circ < \text{RA} < 220^\circ$. This covers the high latitude region $54^\circ < b < 63^\circ$, in the inner Galaxy $312^\circ < l < 347^\circ$. The data has been split into fainter stars $g_0 > 18$ in the top panels and brighter stars $g_0 < 18$ in the bottom panels. The unweighted metallicity distributions show a slight bias to a higher number of metal-poor stars, particularly in the faint bins, which are likely to be predominantly halo stars given these are high latitude fields. Since these fields are towards the inner Galaxy, metal-rich thick disk stars must also be numerous, and the weighting method corrects for this, seen more evidently in the faint bin. The velocity distributions are in general smoothed by the completeness correction.

ilar method of weighting in $g-r$ vs g space to account for the incompleteness in old MSTO stars with spectroscopy in SEGUE’s low galactic latitudes fields. They multiply this weight with additional weights - one based on a luminosity function, to reduce bias against redder metal-rich stars in their sample selection; this was found to be mostly constant, and another based on area covered on the sky to account for regions with high extinction that were not considered for spectroscopy; this does not apply to the WGN data. Liu & van de Ven (2012) analyse G type SEGUE stars and employ weights which are a function of $u-g$, $g-r$ colours and distance. Their distances are determined using relations from Ivezić et al. (2008) and though they state that uncertainties in distance determination will not affect the weights, using apparent magnitude instead avoids this potential problem.

3.1.6 Comparison to Photometric Metallicities

Ivezić et al. (2008) describe a method of estimating metallicities for those F/G main-sequence stars for which spectra have not been obtained in SDSS, from their $u-g$ and $g-r$ colours, to achieve the same goal as above. Building on the classical photometric metallicity calibrations applied to Galactic structure by Sandage & Eggen (1959), Eggen et al.

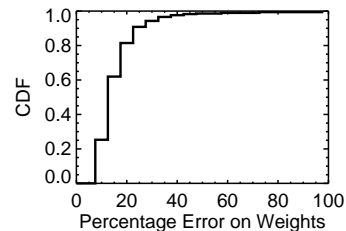


Figure 6. The cumulative distribution function of the percentage errors on the weights assigned to the stars by our weighting method for completeness correction. More than 80% of the stars have less than 20% error, confirming that the completeness corrections derived here are accurate.

(1962), Wallerstein (1962) and Carney (1979), they first use a sample of SDSS stars with spectra to calibrate the metallicities and thereafter use this relation to estimate the metallicities of the complete sample of stars within the same region. The photometric metallicity was calibrated using SDSS DR6 data in the region $0.2 < g-r < 0.6$, $14 < g < 19.5$. The prescription was improved in a follow-up paper by Bond et al. (2010) (hereafter MWIII) replacing the DR6 data by DR7. Their calibration is expected to produce good results in the metallicity range $-2.2 < [\text{Fe}/\text{H}] < -0.2$; at the lower limit, $[\text{Fe}/\text{H}]$ asymptotes due to insensitivity of $u-g$ colour to decrease in metallicity, while at the upper end there is a systematic underestimation of the $[\text{Fe}/\text{H}]$ values, possibly due to a lack of metal rich stars in the calibration data.

Figure 7 shows a comparison between the metallicity distribution functions resulting from WGN metallicities and the photometric metallicities of MWIII for the sample field RA, Dec = $145^\circ, 0^\circ$. Figure 7(a) shows MWIII estimates for those stars which have metallicities directly measured in the WGN survey. We can see that at both high and low metallicities the MWIII method shows large deviations from the measured values. Figure 7(b) more clearly illustrates that MWIII shows systematics of 0.16 dex towards higher metallicities, and very large random errors. The bottom panels show how the metallicity distribution functions (MDF) get affected as a result. While Figure 7(c) shows a comparison between measured WGN metallicities and corresponding photometric metallicities for the same objects, Figure 7(d) compares the weighted distribution function in the same field with the photometric metallicities for the complete SDSS photometric sample in that field. Even though the distributions produced by the two methods do not differ very significantly, the star-by-star comparison shows us that the wings of the MWIII distributions are dominated by large calibration errors. Photometric metallicities, unsurprisingly, blur out the metallicity distribution functions. The photometric MDF in Figure 7(d) looks smooth, while the underlying spectroscopic MDF in the same line of sight suggests a much more discrete halo plus thick disk two-component MDF.

The weighted dataset that we obtain as a result is thus a completeness corrected representation of the WGN selection function.

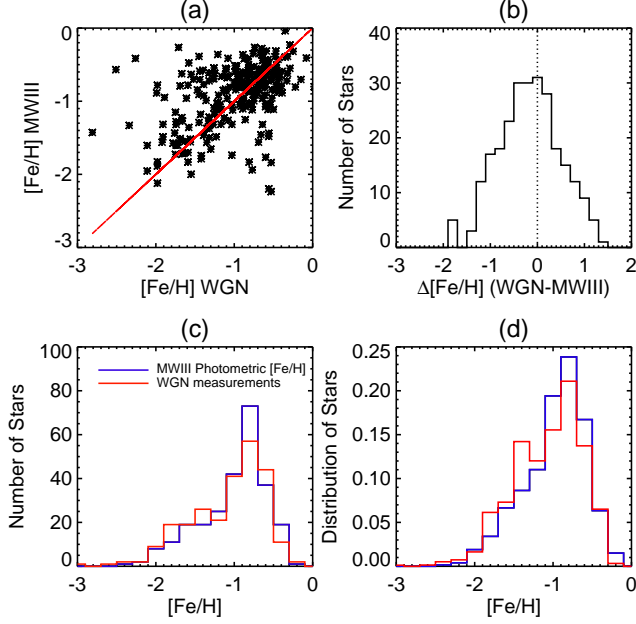


Figure 7. Comparison of WGN metallicities to photometric metallicities from Bond et al. (2010) (referred to as MWIII in the plots) for the sample field RA,Dec=145°,0°. [a] Comparing the measured WGN [Fe/H] to the [Fe/H] calculated for these stars by the photometric metallicity method. The red line shows a one-to-one correlation. [b] Difference between the WGN [Fe/H] and the photometric [Fe/H]. The photometric metallicities have a mean offset of ~ 0.16 dex towards higher metallicities with respect to WGN measurements. The 1σ scatter is 0.68 dex. [c] The observed metallicity distribution function (MDF) from the WGN data compared to the MDF obtained by calculating photometric metallicities for the same stars. [d] Completeness corrected WGN MDF compared to the MDF resulting from calculating the photometric metallicities for the complete SDSS photometric sample in that field.

3.2 Distance Estimates

We now have a completeness corrected dataset of thick disk-halo stars containing information about each star’s position on the sky and radial velocity apart from *ugriz* photometry and metallicity. In order to use this information to analyse the full phase-space structure of the Galaxy we need an estimate of the third position coordinate - distance. Good stellar distance estimates are key to making correct inferences about global Galactic structure.

For Galactic distance scales larger than a few hundred parsec, while we await Gaia, methods of spectroscopic parallax are commonly used to estimate distances. Information on the temperature and metallicity of the stars is used along with stellar evolution models to make an inference about the star’s absolute magnitude and hence deduce its distance given the measured brightness.

In this work we use a χ^2 technique to fit the data to the main sequence of theoretical stellar isochrones in order to estimate distances to the stars. In the following sections we first outline this method, thereafter describing the use of star cluster data to choose the best stellar evolution models, and to test the performance of the method. The errors on the estimated distances are analysed and calibrated. We finally present the distance estimation for the WGN data in

Section 3.2.3. and verify the robustness of these estimates by including the additional constraint of infrared data and comparing to estimates from photometric parallax.

3.2.1 Method

Distances are estimated by a χ^2 fitting of the data to the main sequence of theoretical stellar isochrones. We start with a grid of isochrones with metallicities in the range -2.5 to 0.0 dex such that the choice of the metallicity grid evenly samples colour-magnitude space. The ages of the isochrones are restricted to greater than 10 GYr, since our colour-cut selection ensures that only stars from the old Galactic stellar populations are preferentially selected (the thick disk is estimated to have an age ~ 12 GYrs (Gilmore et al. 1995), while the halo is similarly old with a most recent estimate of inner halo field stars to be $\sim 11.4 \pm 0.7$ GYrs (Kalirai 2012)).

For each set of photometric and metallicity data describing a star, the theoretical isochrones of closest metallicity are first chosen. We then consider those model stars on the chosen metallicity isochrone which are within an $n\sigma$ colour ellipsoid of the data point. The $n\sigma$ bracket was set to optimise the number of stars for which distances are determined.

Let data point j have k model matches within an $n\sigma$ colour ellipsoid. These k matches have the same metallicity (by choice of isochrone) and have varying ages greater than 10 GYrs. The χ^2 value for a data point j with respect to any such model point k is then calculated as follows :

$$(\chi^2)_{model_k}^j = \sum_x \left(\frac{x_{data_j} - x_{model_k}}{\sigma_{x_{data_j}}} \right)^2 \quad (3)$$

where the index $x = \{u - g, g - r, r - i, i - z\}$, each model match k having the associated probability given by,

$$P((\chi^2)_{model_k}^j) = \frac{(\chi^2)^{\frac{m}{2}-1} \exp(-\frac{\chi^2}{2})}{2^{\frac{m}{2}} \Gamma(\frac{m}{2})}$$

where m is the number of degrees of freedom. The luminosity functions appropriate to the isochrones are then used to evaluate the probability $P(M_k | \text{age}_k)$ of a star having an absolute magnitude M_k , as suggested by each model match k , given its age.

The probability assigned to each model star k of being the best match to the data point j is then given by

$$P_{model_k}^j = P((\chi^2)_{model_k}^j) P^j(M_k | \text{age}_k) \quad (4)$$

The closest model match to the star j is then found by maximising $P_{model_k}^j$, and from this absolute magnitude the distance to the star is inferred.

3.2.2 Testing the distance determination method

We use star cluster data with well-known distance estimates to select the set of stellar evolution models which are most consistent with the SDSS photometric data on those clusters, and thereafter to analyse the performance of the method.

3.2.2.1 Star Cluster Data An et al. (2008, hereafter An08) present photometry for stars in 17 globular clusters and 3 open clusters in a value-added catalog of SDSS, derived by reducing SDSS imaging data in crowded cluster fields using the DAOPHOT/ALLFRAME suite of programs. Distances were derived to 6 of these globular clusters and 2 of the open clusters in a subsequent paper by An et al. (2009, hereafter An09) using an isochrone fitting technique in the *ugriz* filter. This reproduced previously available estimates calibrated from Hipparcos parallaxes in the Johnson-Cousins photometric system.

We applied our method to individual stars in five globular clusters looked at by An09 - M5, M3, M13, M92 and M15 ranging in metallicity from -1.26 to -2.42 dex and all older than 12 GYrs - and compared our resulting distance estimates. All these globular clusters have photometry with dependable zero point error from An08. They have [Fe/H] estimates from Kraft & Ivans (2003) based on high resolution spectra. We also chose two open clusters from An08 to cover the metal-rich end of the WGN [Fe/H] range - M67 and NGC2420 with [Fe/H] = 0.00 and -0.37 dex respectively. The data for NGC2420 was presented in An08 but not analysed by An09. Its distance, metallicity and reddening values were adopted by An08 from Anthony-Twarog et al. (2006).

Cluster members were chosen based on a good image quality index, a measured characteristic radius close to that of the chosen PSF in pixels, and by removing pixels with either no detection or saturated detection. The results are discussed below, after we consider the optimal choice of isochrones.

3.2.2.2 Selection of isochrones Several sets of isochrones are available matched to old stars with SDSS photometry. An09, whose distance scale we compare to our own, apply the Yale Rotating Evolutionary Code (YREC; Sills et al. (2000)) isochrones to estimate the star cluster distances. They discount the *u* filter as the models overestimate the flux in the *u* bandpass causing a 5% difference between data and model for colours involving this bandpass. More encouragingly, they find that the YREC model colours in *g-r*, *g-i* and *g-z* agree well with the main sequence of their globular cluster data. They also adopt an alpha-enhancement scheme motivated by the observed amounts of alpha elements in field and cluster stars.

In Figure 8 we compare three sets of isochrones - Dartmouth (Dotter et al. 2008), YREC and Padova (Girardi et al. 2004) - with data for the Globular Cluster M3. M3 has [Fe/H] = -1.50, estimated age = 13.3 ± 1.4 GYrs and estimated distance 9.44 ± 1.03 kpc (An09). All isochrones shown have [Fe/H] = -1.5 and age = 12.5 GYrs (the closest age to that estimated for M3 for which all three models have calculated isochrones). An09 use the YREC isochrone with $[\alpha/\text{Fe}] = +0.3$. The Dartmouth database provides isochrones with a coarse grid in alpha-enhancement, from which we pick two isochrones of $[\alpha/\text{Fe}] = 0$ and $+0.4$. The Padova database does not provide isochrones with alpha-enhancement, so we pick $[\alpha/\text{Fe}] = 0$.

The leftmost panel of Figure 8 plots log luminosity vs effective temperature, and this shows that all three models are in good agreement with each other, with the exception of the systematic deviation of the Padova isochrones on the lower main-sequence, which is not relevant here. The

three isochrone groups employ different methods to convert luminosities and effective temperatures to magnitudes and colours, which is reflected in the next three panels of Figure 8. Here the isochrones have been over-plotted with the data for M3, assuming the distance to M3 is as determined in An09 (i.e. ~ 9.77 kpc).

In the Dartmouth Stellar Evolution Model, the model colours suffer from inaccuracy in synthetic fluxes for central wavelengths bluer than ~ 5000 Å thus making the *u* filter very uncertain. Additionally, problems exist in the underlying SDSS calibration of the *u* and *z* filters, which have larger statistical errors in their zero points and poorer photometric uniformity (both by approximately 50%) as compared to the *gri* filters.² From Figure 8 we see that while the Dartmouth isochrones seem to agree with data in the *g-r* and *g-i* colours, there is a large deviation (almost 0.5 magnitude near the turn-off of the cluster) in *g-z*. This suggests that there are larger errors associated with the model *z* filter, as compared to *gri*. The Padova isochrones seem to have poorer agreement with data both in *g-i* and *g-z* colours.

In addition to good agreement to data in the *gri* filters, the Dartmouth database provide a finer grid of both metallicities (user determined) and ages (0.5 GYrs). Both the Padova and YREC databases have more sparse sampling at higher ages relevant to the WGN data. Thus we adopt the Dartmouth isochrones, excluding the *u* and *z* bandpasses from the isochrone fitting i.e. in Equation 3 we use only colours $x = \{g-r, r-i\}$.

3.2.2.3 Performance The distance determination method was tested on the chosen star clusters by picking the isochrone of the closest [Fe/H] to the cluster. For all the globular clusters, the age of the isochrones was restricted to above 12 GYrs. Matches within a 2σ ellipse of two colour filters *g-r* and *r-i* was used in the χ^2 fitting. A 2σ ellipsoid was sufficient to obtain distances for at least 80% of the cluster data.

The performance of the distance determination method can be analysed by means of an example case of M13 shown in Figure 9. The leftmost panel shows a CMD of the cluster containing all cluster members for which distances were determined. The second panel from the left shows a plot of *g-r* vs the absolute *g* magnitude assigned to the star by the distance determination method. The third panel from left shows the deviation of this distance estimate from the “true” (An09) distance of the cluster as a function of apparent magnitude *g*. This panel has been colour coded to highlight groups of stars which show extremely deviant distances. These deviant groups are as follows:

- The red points mark the giant stars (i.e stars having apparent magnitude *g* brighter than turn-off) but are incorrectly assigned to be main sequence stars by the routine. As a result, their distances are underestimated. These are isolated using a rough cut of $g < 19$ and absolute *g* magnitude $> \sim 4$.
- The light-blue plus signs on the contrary are main sequence stars (i.e stars having apparent magnitude *g* fainter than turn-off) that have been incorrectly assigned to be giants, thus overestimating their distances. These are isolated

² <http://www.sdss.org/dr7/algorithms/fluxcal.html>

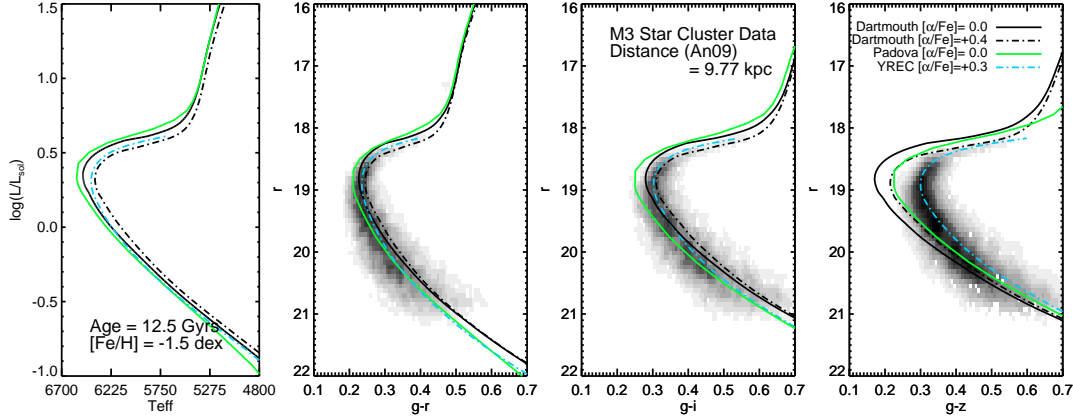


Figure 8. We compare stellar evolution models to star cluster data. Three sets of isochrones - Dartmouth, YREC and Padova - are compared with the SDSS photometric data for the globular cluster M3. The adopted properties of M3 are: $[\text{Fe}/\text{H}] = -1.50$, age = 13.3 ± 1.4 GYrs, distance (An et al. 2009) 9.44 ± 1.03 kpc. All isochrones shown have $[\text{Fe}/\text{H}] = -1.5$ and age = 12.5 GYrs (the closest age to that of M3 which has isochrones in all three models). The YREC isochrone has $[\alpha/\text{Fe}] = +0.3$; two Dartmouth isochrones with $[\alpha/\text{Fe}] = 0$ and $+0.4$ are shown; the Padova isochrone has $[\alpha/\text{Fe}] = 0$. The leftmost panel plots $\text{Log} L$ vs T_{eff} , and this shows that all three models are in good agreement with each other in the luminosity region of relevance here. The different approaches to convert luminosities and effective temperatures to magnitudes and SDSS colours are reflected in the next three panels, where the isochrones have been over-plotted with the SDSS photometric data for M3. From this comparison we adopt the Dartmouth isochrones restricting their application to $g-r$ and $g-i$ colours.

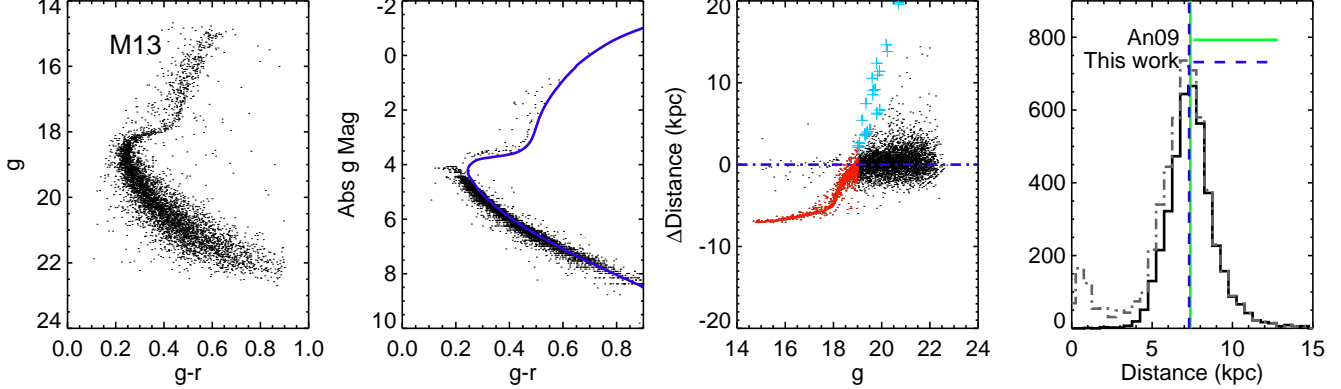


Figure 9. Results of our distance determination method applied to the globular cluster M13. The left most panel shows the CMD of the cluster, the second panel from left shows the absolute g magnitude recovered for each star from the isochrone fitting, the third panel from left shows the deviation of estimated distance from the An09 value as a function of apparent magnitude g (red points mark giants mis-classified as main sequence stars; blue plus signs mark the main sequence stars which are mis-classified as giants) and the rightmost panel shows the distance distribution recovered by the method for all stars (grey dashed line) and for correctly classified main sequence stars (solid black line)

using a rough cut of absolute g magnitude up to the value of 4.

Apart from these anomalies, good estimates of distances are assigned to the bulk of the main sequence stars shown in black. This can be seen more clearly from the rightmost panel in Figure 9 (solid black line) which shows the distance distribution recovered for the cluster after eliminating all the anomalous star groups (blue and red points) as described above. The blue dashed vertical line which indicates the mean distance estimated for the cluster by our method matches the green line which indicates the value estimated by An09 within 5%. The 1σ spread of the distribution is

1.1 kpc (placing $\sim 70\%$ of the stars within 15% of the mean distance).

In Figure 10(a) we show the results of testing the distance determination method at the metal rich end. All panels are the same as in Figure 9. There are no giants in the cluster, and hence no red points. The blue plus signs mark out the main sequence stars mistakenly assigned to be giants, as before. But the noticeable difference now is that *all* main sequence stars up to a $g-r$ colour of 0.6 (which is the relevant $g-r$ colour range for the WGN data) seem to be mis-assigned as giants. The reason for this can be understood from the form of the Luminosity Function for high metallicities - for the higher metallicities, the probability of

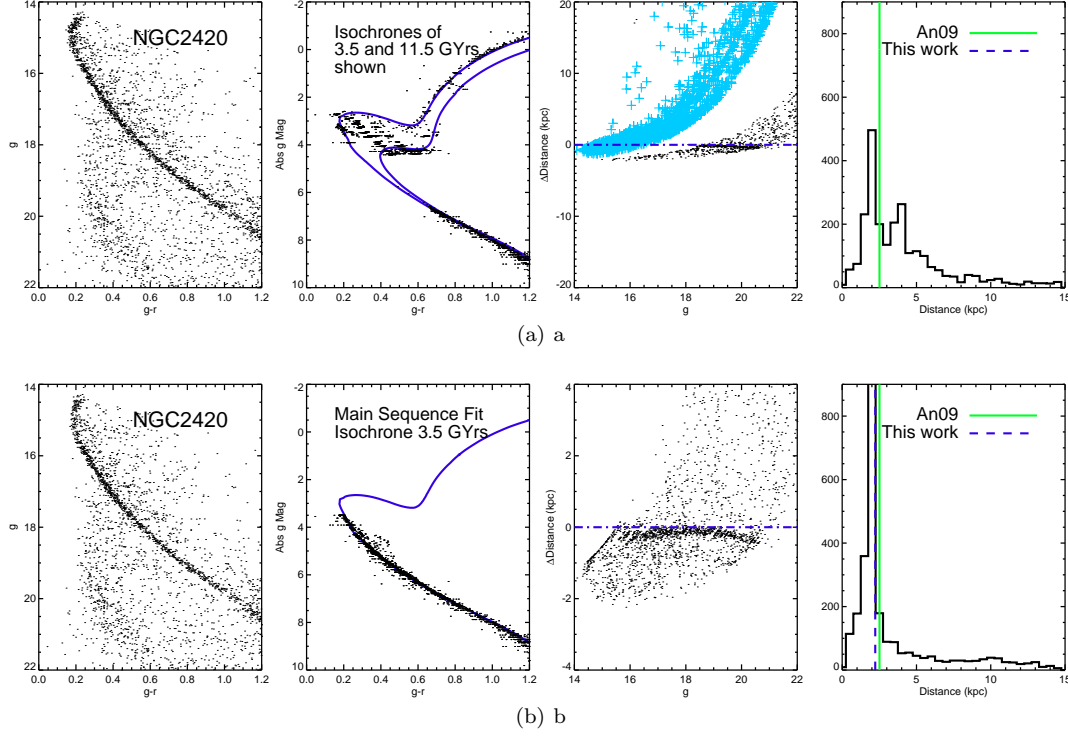


Figure 10. Results of our distance determination method applied to the open cluster NGC 2420 ($[\text{Fe}/\text{H}] = -0.37\text{dex}$, Age ~ 3.5 GYrs). (a) Top panels : Results on applying isochrone fit, restricting ages to above 3.5 GYrs. In this case almost all stars below $g - r = 0.6$ are incorrectly assigned to the sub-giant branch. (b) Bottom Panels : Results on applying isochrone fit, restricting ages to above 3.5 GYrs and additionally restricting the fit to the main sequence region only. Here the problem of mis-classification of main sequence stars is resolved. In both (a) and (b), the left most panel shows the CMD of the cluster, the second panel from left shows the absolute g magnitude recovered for each star from the isochrone fitting, the third panel from left shows the deviation of estimated distance from the An09 value as a function of apparent magnitude g (blue plus signs mark the main sequence stars which are mis-classified as giants) and the rightmost panel shows the distance distribution recovered by the method for correctly classified main sequence stars.

finding a star near turn-off or on the sub-giant branch is equal to (or more than) that of finding a star on the Main Sequence, as against the lower metallicities where the probability steadily decreases from lower main-sequence going towards turn-off. Since we use the luminosity function as an additional constraint to determine the absolute magnitude assigned to a star, all main sequence stars are identified as sub-giants at high metallicities.

Given the WGN data is comprised mainly of main sequence (mostly turn-off) stars, we can remedy this problem by forcing the program to choose model stars that only lie on the main sequence (placing a cut-off at turn-off). The result of this is illustrated in Figure 10(b). We immediately see that all the main-sequence stars are now assigned good distances and the recovered mean distance is within 10% of the An09 value.

While Figures 9 and 10 illustrate convincingly that the method always recovers the correct distance for the cluster as a whole, Figure 10(b) also reveals that the mean recovered distance could be a weak function of the photometry itself. This trend is further discussed and calibrated in Section 3.2.2.4.

Our estimated cluster distances, together with those adopted for comparison, are summarised in Table 2, along with the various cluster parameters. We see that our method

reproduces star cluster distances within 10% of the distance scale adopted by An09.

3.2.2.4 Result and Calibration of Errors As noted in section 3.2.2.3, while the mean distance recovered for the cluster by the distance determination method matches well with the true distance, there is a weak trend of the recovered distance with photometry. There is also an error which is introduced due to the finite $[\text{Fe}/\text{H}]$ grid that is chosen. In this section we analyse and calibrate these different contributions to uncertainty in our distance estimates to individual stars.

(i) Distance error due to photometric errors

Figure 11 (top and middle panels) shows the dependence of error in distance on error in $g - r$ colour, derived from analysis of the photometry for the five globular clusters. We calibrate errors based only on the old globular clusters as these are more comparable to WGN data in age than are the open clusters. Although the photometric uncertainties for our field stars are typically less than 3%, for the crowded fields of star clusters errors can be larger, allowing sufficient dynamic range for this test. On average, 80% of the cluster stars have σ_{g-r} less than 0.1.

The systematic trend in the dispersion of distance errors at small σ_{g-r} is due to two reasons. The dominant effect is the systematic mis-identification of sub-giant stars

Table 2. Star Clusters used to test the distance determination method

Cluster	[Fe/H]	Distance (kpc)	E(B-V)	Age (GYrs)	Dartmouth Isochrone [Fe/H]	Result Mean Distance	% Error
Globular Clusters							
M5	-1.26	7.11 ± 0.20	0.03	12.2 ± 1.3	-1.20	7.36	4
M3	-1.50	9.77 ± 0.32	0.01	13.3 ± 1.4	-1.50	9.58	2
M13	-1.60	7.37 ± 0.18	0.02	14.3 ± 1.1	-1.60	7.30	1
M92	-2.38	8.55 ± 0.15	0.02	14.4 ± 0.9	-2.40	8.64	1
M15	-2.42	10.47 ± 0.55	0.10	13.5 ± 2.5	-2.40	9.87	5
Open Clusters							
M67	0.00	0.82	0.03	3.5	0.00	0.84	2
NGC2420	-0.37	2.51	0.04	3.5	-0.40	2.23	11

near the turn-off as main-sequence stars below the turn-off, which produces systematically offset distances. The second, and smaller, of the two effects is the systematic sensitivity to age near the turn-off, with the method showing some bias to younger isochrones weighted by a higher probability from the luminosity function. Not surprisingly, restricting the isochrone search to the age adopted for the parent cluster diminished the distance bias. Of course, a single age cannot be applied to the mixed population field star WGN data, for which only a reasonable lower limit of age can be imposed. This distance bias, though, defines our error limits, and is sufficiently small as not to limit our later analysis.

(ii) Distance error due to uncertainty in [Fe/H]

In our method, we have assumed that the [Fe/H] estimate is accurate, and hence choose the isochrone with metallicity closest in value to this measured value. Here we quantify the uncertainty in the distance introduced by uncertainties in metallicity, which we determined to be ~ 0.2 dex in [Fe/H]. We do this by applying the distance determination method to the stars in the test clusters while varying the [Fe/H] of the chosen isochrone around the best value. The bottom panel of Figure 11 shows the results in the case of four of the globular clusters (M15 is not shown here as it has same [Fe/H] as M92). The WGN and SDSS data, to which our method will be applied, have [Fe/H] accuracies ~ 0.2 dex, and from the figure we determine that the systematic error on distance due to 0.2 dex uncertainty in [Fe/H] is within 10%.

(iii) Distance error due to luminosity mis-classification of stars

By restricting the isochrone fit only to the main sequence region, we ensure that no main sequence star is mis-classified as a giant (as illustrated in Figure 10(b)). But the sub-giants in the WGN data near turn-off are mostly (more than 95%) mis-classified as main sequence stars (as illustrated by the red points in Figure 9). From point (i) in this section we have shown that there is a systematic error due to this mis-classification of sub-giants near the turn-off of within 10%. From Figure 9 we note that for sub-giants redder than turn off the distance errors can blow up to as large as 50%.

We also note that in the case of clusters M5 and M92, there is no upward trend in errors near small σ_{g-r} , as compared to the noticeable trend in M3, M13 and M15. This is

because of the presence of fewer giants (less than 0.5%) in the data of the former two globular clusters, as compared to the latter in which more than 4.5% of the cluster members are giants.

The fraction of a field star sample which will be sub-giants rather than MSTO stars was a popular topic of discussion in the 1980's star-count literature. Some of many papers discussing the issue include Bahcall et al. (1985), Gilmore et al. (1995), Fenkart (1989), and Gilmore et al. (1989). All are consistent with results that can now be readily reproduced using the on-line Besançon star count model as shown in Figure 12. This confirms that sub-giant contamination in a colour and magnitude selected survey of thick disk and halo stars with photometric criteria like those of this WGN sample will be typically at the 5% to 10% level, increasing to 13-15% in some lines of sight.

Thus we can say that sub-giants, certainly present in the WGN data, will be mis-classified as main sequence turnoff stars, introducing a systematic underestimation of their distance by 20 to 50%. We expect this contamination from sub-giants to be small (below 10% per field) and thus not affect our present analysis in a significant way.

3.2.3 Distance estimates for the WGN data

We thus derive distances for stars in the WGN dataset via the isochrone fitting method described above using $g-r$ and $r-i$ colours. We use a set of 17 isochrones from the Dartmouth Stellar Evolution Database (Dotter et al. 2008) for metallicities in the range -2.5 to 0.0 dex (and no alpha-enhancement), such that the choice of isochrones evenly samples colour-magnitude space. We fit to only the main sequence of the isochrones and restrict their ages to greater than 10GYrs. The corresponding luminosity functions (age and metallicity dependent) were adopted from the same database. A 4σ colour bracket was required to find matches for lower main sequence stars with small σ_{g-r} where the isochrone sampling is sparse. Distances could be estimated for 8965 objects out of the 9404 in the sample. The few hundred stars for which the routine was unable to determine distances are those which do not fall on the thick disk/halo CMDs either because they are extreme blue stars ($g-r < 0.2$) or because they are likely binaries, variables or

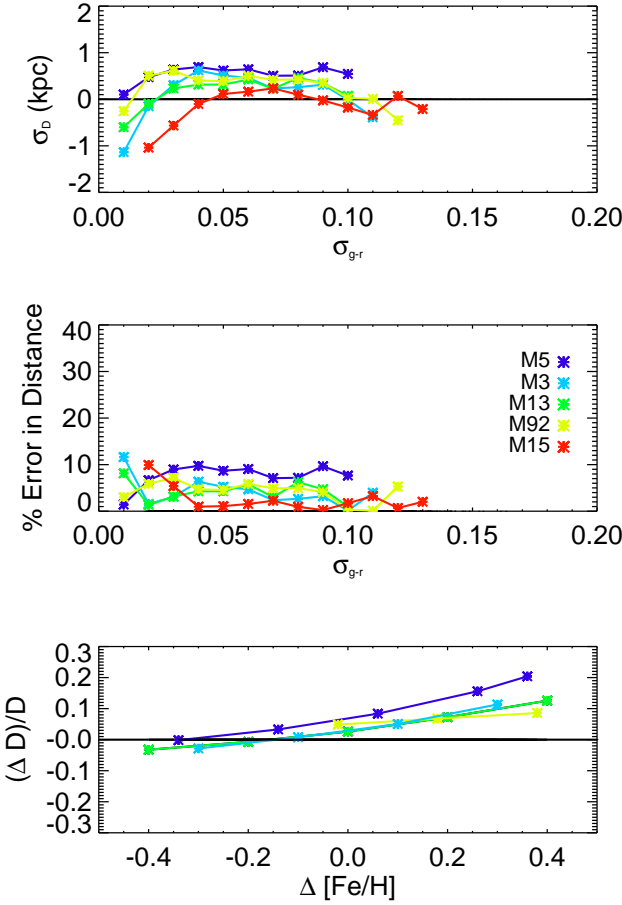


Figure 11. Errors in distance estimation, as a function of uncertainties in photometry and metallicity, are plotted for five star clusters (M5, M3, M13, M92 and M15). Top panel: the dispersion, and Middle panel: the percentage error in distance due to errors in the single-star photometry. The bias in the dispersion at small σ_{g-r} is due to the mis-identification of sub-giant stars near the turn-off as main-sequence stars. Lower panel: The error in distance due to a systematic error in metallicity, determined by applying the distance determination method to the star cluster photometry while adopting an isochrone with $[\text{Fe}/\text{H}]$ offset from the notional cluster value. The systematic distance error corresponding to 0.2dex uncertainty for $[\text{Fe}/\text{H}]$ is less than 10%.

have mis-calibrated metallicities. The prior assumed for the age (older than 10GYrs) also produces a bias against metal-rich stars. The distance distribution peaks at just above 2 kpc, most stars being within a heliocentric distance of 6 kpc.

We now consider adding additional photometric information, as a further test of distance scale systematics.

3.2.3.1 Including infrared photometry - testing systematic distance bias In order to further check the robustness of our distance estimates, particularly against systematic bias, we tested the value of incorporating infrared photometry into the isochrone fitting, combining J-, H- and K-band data with the *gri*-band data.

UKIDSS may be considered as the near-infrared counterpart of the SDSS Imaging survey (Hewett et al. 2006).

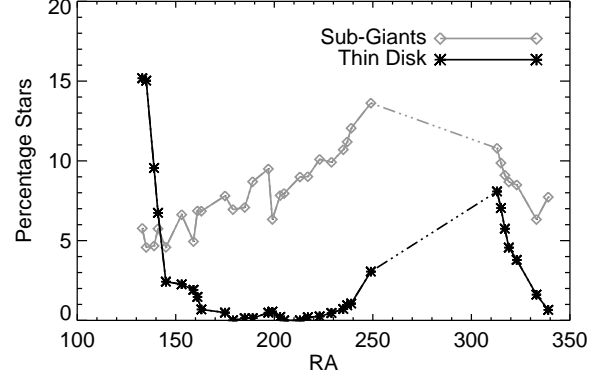


Figure 12. Percentage of sub-giants (Grey Diamonds) and thin disk (Black asterisk) stars in each field as produced by the Besançon Model of the Galaxy on application of the WGN selection function. This gives an estimate of the expected contamination from subgiants and thin disk for a colour and magnitude selected survey of thick disk and halo stars with photometric criteria like those of this WGN sample. The plot confirms that sub-giant contamination in the WGN sample will be typically at the 5% to 10% level, increasing to 13-15% in some lines of sight (discussed in Section 3.2.2.4). It also shows that thin disk contamination is expected to be minimal in the WGN sample (discussed in Section 4.3), ranging between 5 and 15% in the low latitude fields (i.e near $\text{Ra} \sim 133^\circ$, $\text{Ra} \sim 249^\circ$ and $\text{Ra} \sim 313^\circ$).

The Large Area Survey (LAS) covers 4000 sq. deg. at high Galactic latitudes, with imaging in YJHK filters to a depth of $K=18.4$. This coverage includes a LAS equatorial block which overlaps with most of the sky coverage of the WGN survey.

We cross-matched the WGN dataset with the UKIDSS LAS data. This provided 3409 matches out of 9404 stars in WGN. We used the JHK filters in tandem with the *gri* filters to estimate the distances by our isochrone fitting method i.e. we now use $x = g - r, r - i, J - H, J - K$ in Equation 3. The distance determination proceeded as described above. We compare the new distance estimates, obtained using JHK both independently and with *gri*, referred to as D_{JHK} and D_{griJHK} , to the distance estimates from just *gri* (D_{gri}) in Figure 13.

We see that D_{JHK} shows a mean offset of 0.08 kpc with respect to D_{gri} , though with a large scatter of $1\sigma = 0.48$ kpc. This greatly improves in the case of D_{griJHK} where the mean offset reduces to -0.03 kpc and a much tighter spread of $1\sigma = 0.17$ kpc. This shows that there is no bias in the estimated distances using *gri* relative to the combined optical-infrared approach. In this same figure, we also illustrate the effect of retaining the *z* filter in the left most panel. $D_{gri z}$ has a systematic bias, being offset by around 0.2 kpc from D_{gri} .

Thus by comparing our distance estimates with those obtained using tighter constraints (i.e. using *JHK* along with *gri*), we confirm that there is no systematic bias in our distances.

3.2.3.2 Comparing isochrone-fit distances with photometric parallax distances We also compared our

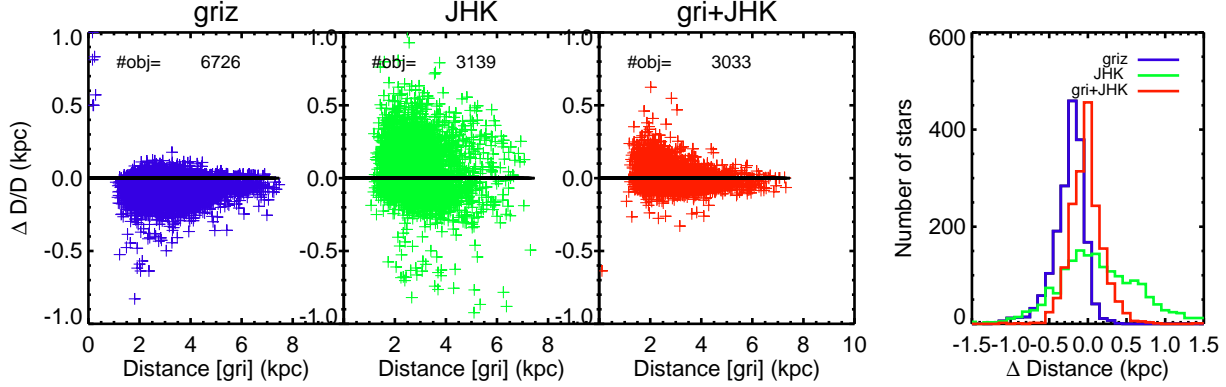


Figure 13. This figure compares isochrone-fit distance estimates using optical only, infrared only, and combined optical plus infrared photometry. The first three panels plots the relative error in distance estimates from using *griz* filters (blue), the UKIDSS infrared JHK filters (green) and by combining the *gri* and JHK filters (red) with respect to distance estimates using *gri* filters (D_{gri}). D_{griz} has a systematic bias, being offset by around 0.2 kpc from D_{gri} . D_{JHK} shows a mean offset of 0.08 kpc with respect to D_{gri} , though with a large scatter of $1\sigma = 0.48$ kpc. This greatly improves in the case of $D_{gri+JHK}$ where the mean offset reduces to -0.03 kpc and a much tighter spread of $1\sigma = 0.17$ kpc.

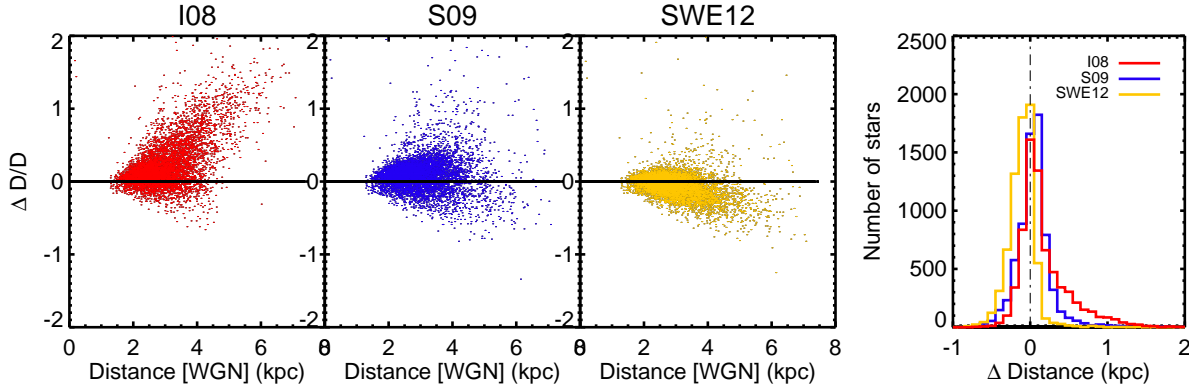


Figure 14. We compare the photometric parallax method of estimating distances to the isochrone fitting technique used in this work. In the first three panels distance estimates from our isochrone fitting method are compared to distances from photometric parallaxes, using the recipes prescribed in Ivezić et al. (2008) (red), Smith et al. (2009) (blue), and Smith, Whiteoak & Evans (2012) (orange) in terms of relative distance error. I08 systematically overestimates the distances with an average offset of ~ 0.09 kpc, showing larger deviations at larger distances. The match improves in the case of S09 with a mean offset of ~ 0.08 kpc, while the SWE12 method matches the distances computed in this work most closely. The mean offset with respect to SWE12 is ~ -0.04 kpc, with a spread of ~ 0.12 kpc.

distances to those obtained by applying the method of photometric parallax used by Ivezić et al. (2008) (hereafter I08). In this method, an empirical relationship between absolute magnitude and colour is first adopted, which is independent of both age and metallicity and only describes the *shape* of the colour-magnitude sequence below turn-off. This zeroth-order relationship is usually adopted by finding the best-fit function to the CMD of a globular cluster of known abundance and whose distance is known fairly accurately by means of some other reliable method of distance measurement. Then correction terms are introduced which shift this relation to represent the true age and metallicity.

I08 perform an empirical fit simultaneously to the photometry of stars of five globular clusters from SDSS to obtain the basic photometric parallax relation. They then use the M13 globular cluster to determine the correction term due to the effect of age on the CMD. This age correction is cal-

culated under the constraint of a fixed value of metallicity - which in their case is the mean metallicity of M13 ($[\text{Fe}/\text{H}] = -1.54$), which is close to the mean metallicity of the Galactic halo. Strictly speaking, this will not hold for thick disk stars whose mean metallicity, at least in local samples, differs by the order of $+1.0$ dex from that of halo stars, even if the two populations have approximately the same age, within an uncertainty of 2 Gyr. I08 adopt this correction on the basis that this will produce an error of less than 0.2 mag for disk-like stars (which corresponds to an error in distance estimate of 1 kpc in our case). Smith et al. (2009) (hereafter S09) propose an improved correction which takes into account that the morphology of the colour-magnitude relation near turn-off depends significantly on both age and metallicity. More recently Smith, Whiteoak & Evans (2012) (hereafter SWE12) modified this to construct a global turn-off correction applicable to a mixture of disk and halo stars.

All the above methods were applicable in the colour region of $0.3 < g - i < 0.6$. This colour restriction eliminates close to 2000 stars from the WGN dataset, the majority of these being thick disk turn-off stars with $g - r \geq 0.6$.

Selecting only those stars from the WGN dataset which fall in the photometric calibration $g - i$ colour range, the distances computed here using our isochrone matching technique may be compared to the values obtained by applying the methods of I08, S09 and SWE12. The comparison is shown in Figure 14. I08 systematically overestimates the distances to the stars, with larger deviations at larger distances. The I08 values are on average offset from distances from this work by ~ 0.09 kpc. The match improves in case of S09 with a mean offset of ~ 0.08 kpc, while the SWE12 method match the distances computed in this work most closely. The mean offset with respect to SWE12 is ~ -0.04 kpc, with a spread of ~ 0.12 kpc.

This provides a final consistency check on our distance estimates.

The method of photometric parallax works well in the case of faint main-sequence stars and single stellar population, but is limited by the availability of calibration stars over a large range of stellar mass and metallicity. In the case of a mixture of populations, the age correction in the photometric parallax method requires an assumption about the fraction of stars from different populations which S09, for example, determine based on a kinematic and chemical segregation of stars. Our method based on stellar evolution models avoids any such assumption and is more robust in accounting for the age and metallicity effects for turn-off stars.

We thus have estimated distances to 8965 stars in the WGN dataset, with 90% of them having uncertainty within 10%.

Figure 15 shows the spatial coverage of the data. The data covers a range of Galactocentric radii (projected distance on the plane) between 4 and 12 kpc. There is also coverage above and below the Galactic plane, extending up to a height of 6 kpc. This provides the scope to investigate radial and vertical gradients in the abundance and kinematic parameters, as well as to investigate spatial distributions in a coherent way. The coverage of the data on the Galactic plane, shown by the X vs Y plot, shows the potential of the data to investigate symmetries in the Galaxy - about the plane, about the cardinal direction $l \sim 270^\circ$ and about the centre of the Galaxy.

3.3 Proper Motions and Global Space Velocities

Proper motions (along RA and Dec) for the WGN stars are available from SDSS DR7. Using these along with the distance estimates obtained as described in the previous section and the measured radial velocities, we can obtain right-handed Galactic U, V, W velocities using the conversion outlined in Johnson & Soderblom (1987). These are then converted to cylindrical coordinates V_R, V_ϕ, V_Z by simply rotating the coordinate system about the W axis.

In the cylindrical coordinate system, the contribution of the three velocity components to the line of sight (LOS) velocity at any point in space specified by the Galactic longitude l , Galactic latitude b and distance from the sun D are given as

$$V_{LOS} = A_R V_R + A_\phi V_\phi + A_Z V_Z \quad (5)$$

where

$$A_R = \sin(\alpha) \cos(b) \quad (6)$$

$$A_\phi = \cos(\alpha) \cos(b)$$

$$A_Z = \sin(b)$$

and where α is the angle between V_ϕ and the line of sight direction which depends on l, b and D and is given as follows:

$$\alpha = \pi - l - \theta_{GC} \quad (7)$$

$$\text{where } \theta_{GC} = \tan^{-1} \frac{D \cos(b) \sin(l)}{R_0 - D \cos(b) \cos(l)}$$

and R_0 is assumed to be 8.5 kpc (Kerr & Lynden-Bell 1986).

Here, V_{LOS} is the line of sight velocity component in the rest frame of the Galaxy which is related to the measured heliocentric radial velocity V_{hel} by

$$V_{LOS} = V_{hel} + V_{corr} + V_{LSRcorr} \quad (8)$$

where V_{corr} corrects for the peculiar motion of the sun [we adopt $(U_\odot, V_\odot, W_\odot) = (11.1, 12.2, 7.2)$ km/s (Schönrich et al. 2010)] with respect to the Local Standard of Rest

$$V_{corr} = U_\odot \cos(l) \cos(b) + V_\odot \sin(l) \cos(b) + W_\odot \sin(b) \quad (9)$$

and $V_{LSRcorr}$ converts the measured quantity into the rest frame of the Galaxy:

$$V_{LSRcorr} = V_{LSR} \sin(l) \cos(b) \quad (10)$$

V_{LSR} has been taken to be 220 km/s (Kerr & Lynden-Bell 1986).

Given the spatial distribution of stars in our dataset, the relative contributions of the three Galactic Space velocity components to the measured line of sight velocity varies widely across the fields. The contribution of V_ϕ goes to zero in the direction towards the Galactic Centre, while the V_R contribution goes to zero perpendicular to this direction ($l \sim 90^\circ$ and 270°). This is reflected in the variation of uncertainties in the velocities of each of these components along Galactic longitude. While V_R is most accurately determined towards the Galactic centre from V_{LOS} alone, V_ϕ is more reliably determined in the perpendicular direction.

In this work, we are particularly interested in the global behaviour of the V_ϕ parameter, as this is a primary thick disk-halo discriminator. Since the sensitivity of the line of sight velocity to V_ϕ varies considerably across our fields, large errors in proper motion can significantly distort the true V_ϕ distribution. Figure 16 analyses the contribution of errors from the two different sources, namely from distance and proper motion errors, to the V_ϕ distribution. Considered in this figure are only fields centred on the cardinal direction $l = 270^\circ$, which makes the observed radial velocity more sensitive to V_ϕ as compared to V_R . The leftmost figure shows the distribution of the computed V_ϕ if both distance and proper motion measurements are considered to be accurate. The middle and rightmost plots show how the Probability Distribution Function (PDF) is altered if there is a contribution of error from only distances and only proper motions respectively. The typical errors in proper motion are around 3 mas/yr while typical errors in distance are 0.2 kpc. When considering errors only from proper motions (i.e.

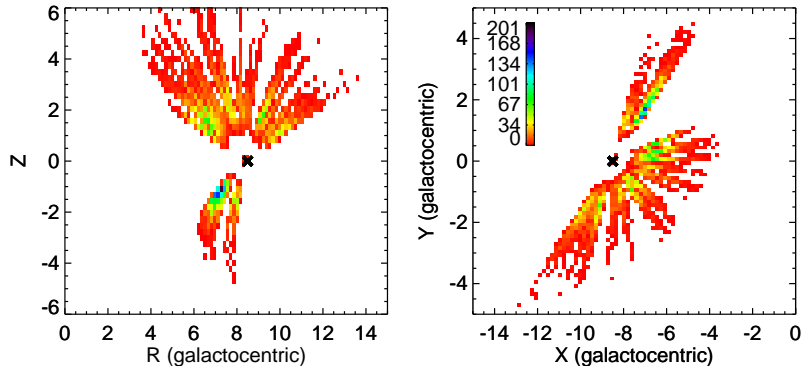


Figure 15. The spatial extent of the WGN survey data in XYZR galactic coordinates. In both plots, the black cross shows the position of the Sun. Colours indicate the number of stars in each spatial bin, colour coded as shown.

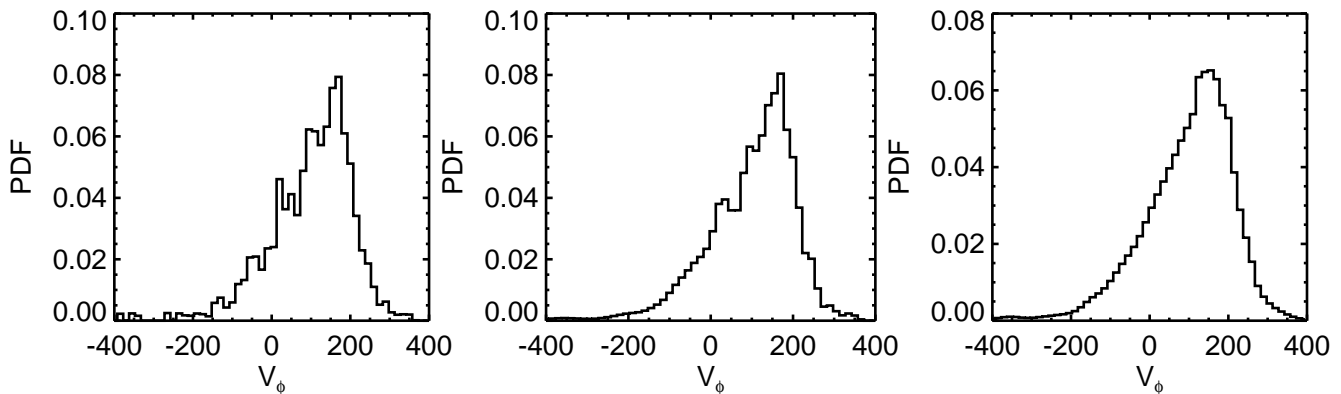


Figure 16. Space motion error analysis for fields in the direction $l = 270^\circ$. Left Panel: V_ϕ distribution derived using radial velocity, proper motions and distance, while assuming that there are zero errors on distance and proper motions. Middle panel: V_ϕ distribution when convolved with the contribution of error from distances alone (i.e. setting $\sigma_{\mu_\alpha}, \sigma_{\mu_\delta} = 0$). Distance errors are less than 10%, thus ensuring that 80% stars have less than 10% error on V_ϕ . Right panel: V_ϕ distribution when convolved with the errors from proper motions alone (i.e. $\sigma_D = 0$) which are typically 3mas/yr resulting in 85% stars having greater than 20% error on V_ϕ . Evidently proper motion uncertainties dominate the error budget.

setting $\sigma_D = 0$) only 15% of the stars have σ_{V_ϕ} within 10%. The typical errors on V_ϕ are $\sim 13\%$. Almost 40% of the stars have errors on V_ϕ greater than 20% thus smearing out the distribution on the rightmost panel of Figure 16. In contrast, when considering errors only from distances (setting $\sigma_{\mu_\alpha}, \sigma_{\mu_\delta} = 0$) 80% of the stars have σ_{V_ϕ} better than 10% with typical errors of 3%.

This clearly illustrates that proper motions are the chief contributors to errors in the velocity components, a factor we consider in the analysis below.

4 ANALYSIS

We now proceed to analyse the WGN survey data, considering in turn the validity and numerical values of single parametric descriptions of the thick disk, for kinematics and spatial scale length. We then consider, and discover, spatially localised substructure in the survey.

4.1 Kinematic and Number-Density Modelling in Observable Space

When analysing a set of distances, abundances and kinematics for a mix of stellar populations one approach is to minimise error propagation by looking for models in physical space that most closely reproduce probability distribution functions in observable space. In our sample, the radial velocities are of higher internal precision than are the other contributions to space motions (cf. Figure 16), so we proceed accordingly.

We model the data in the one dimensional space of line of sight velocity V_{LOS} . The data are assumed to be completely described by a two-component model consisting of the thick disk (denoted as TD) and the halo, using the discussion associated with the selection function earlier to justify exclusion of thin disk populations. Initially, the three cylindrical velocity components i.e. V_R, V_ϕ, V_Z are assumed to be distributed as Gaussians for the thick disk and halo independently.

A maximum likelihood method is employed to deter-

mine the best model given the data. The likelihood of a particular model Φ given n data points $X = x_1, x_2, \dots, x_n$ is then given by

$$L(\Phi|X) = \prod_1^n P(x_i|\Phi) \quad (11)$$

where

$$\begin{aligned} P(x_i|\Phi) &= fP(x_i|\Phi^{TD}) + (1-f)P(x_i|\Phi^{halo}) \\ &= fP(\Phi^{TD}(V_{LOS,i}|V_{LOS})) \\ &\quad + (1-f)P(\Phi^{halo}(V_{LOS,i}|V_{LOS})) \end{aligned}$$

with f being the normalisation of the thick disk component with respect to the total number of stars.

Since we do not know the shape of the distribution of V_{LOS} we can recast this in terms of V_R, V_ϕ, V_Z which have (assumed) Gaussian distributions, and then marginalise over the unknown parameters. This is done using the method outlined in Sirko et al. (2004) in their Appendix A.

The probability of observing a star with a line of sight velocity between V_{LOS} and dV_{LOS} is given by

$$\phi(V_{LOS})dV_{LOS} = \int_{-\infty}^{\infty} \int_{-\infty}^{\infty} \phi_R(V_R)\phi_\phi(V_\phi)\phi_Z(V_Z)dV_RdV_\phi dV_Z$$

with

$$\phi_x(V_x)dV_x = \sqrt{\frac{1}{2\pi\sigma_x^2}} \exp\left(-\frac{(v_x - \mu_x)^2}{2\sigma_x^2}\right). \quad (12)$$

Using the form of V_{LOS} given by equation 5, equation 12 can be analytically solved to obtain the following simple solution

$$\phi(V_{LOS}) = \frac{1}{\sqrt{2\pi\Sigma}} \exp\left[-\frac{\lambda^2}{2\Sigma}\right] \quad (13)$$

where

$$\Sigma = \sigma_R^2 A_R^2 + \sigma_\phi^2 A_\phi^2 + \sigma_Z^2 A_Z^2,$$

$$\lambda = -V_{LOS} + \mu_R A_R + \mu_\phi A_\phi + \mu_Z A_Z$$

with A_R, A_ϕ, A_Z being defined in Equation 6.

The best relative normalisation f is obtained independently for each field for any given configuration of all the other four free parameters.

4.2 Maximum likelihood determination of the thick disk kinematic parameters

In this analysis we seek first to find a maximum likelihood description of the velocity components of the thick disk. The free parameters in the model are μ_{V_ϕ} (henceforth written simply as V_ϕ) and $\sigma_{V_R}, \sigma_{V_\phi}, \sigma_{V_Z}$ of the thick disk, and f , the relative number of thick disk stars to halo stars for each field. All kinematic parameters describing the halo, together with the mean Z and R velocities of the thick disk, are held as fixed parameters in the model. The mean Z and R velocities of the thick disk and mean motions of the halo are set to zero, assuming equilibrium and that there is no net rotation in halo. All those ~ 8900 stars with good photometry, $\sigma_{g-r} \leq 0.1$ and weight error less than 50% were included in the modelling. To ensure kinematic parameters appropriate to SDSS survey results covering comparable volumes to those investigated here, we adopt the values of the velocity

dispersions of the inner halo determined by Carollo et al. (2010). These values are summarised in Table 3.

Figure 17 shows the Galactocentric velocity distribution for the data and the corresponding distribution produced by the best fit model resulting from our maximum likelihood analysis, where the best fit values were found by scanning through parameter space with a step size of $\mu, \sigma = 1, 1$ km/s. In this plot, the number of stars is normalised to be the same in each field in order to pick out features easily by eye. The best fit parameters recovered by the Maximum Likelihood modelling were $V_\phi, \sigma_{V_\phi} = 172, 49$ (km/s) and $\sigma_{V_R}, \sigma_{V_Z} = 51, 40$ (km/s). The rotational velocity is only marginally lower than a canonical thick disk rotation (~ 180 km/s, Carollo et al. (2010)). The contour plots localising maxima and indicating error bounds and parameter correlations for the various parameters are shown in Figure 18. These figures show that this simple kinematic model is a good global description of the data, while our best-fit kinematic parameters are in good agreement with earlier determinations (e.g. Carollo et al. (2010), Chiba & Beers (2000)).

The significance of the difference between model and data (i.e difference between model and data divided by the Poisson error in number counts in each pixel) is plotted in the bottom-most panel of Figure 17. A significant mismatch, which we define as several adjacent pixels each of which is more than 2σ from the model with the same sign, is evident only near $RA \sim 313^\circ$. Here many stars seem to have higher line of sight velocities than predicted by the model.

The region of mismatch covers $312^\circ \leq RA \leq 318^\circ$. It spans low, southern latitudes $-30^\circ \leq b \leq -26^\circ$ and lies in the inner Galaxy $48^\circ \leq l \leq 50^\circ$. It has radial velocities ~ 20 km/s higher than do the typical thick disk stars in these lines of sight. Hereafter, we will refer to this region as R313.

4.3 Sub-structure in the Galactic thick disc?

Is the mismatch seen between the global best-fit kinematic model and the data due to substructure in the thick disk, or is it just an artefact of incorrect extinction or systematic errors in distance? Are the stars with high radial velocity with respect to the thick disk just high contamination from thin disk stars at these low latitudes? We analyse the possibilities in this section.

R313, being at the lower Galactic latitude range of the WGN fields that looks into the inner parts of the Galaxy, is likely to have a larger contamination of thin disk stars. The high rotational velocity of the thin disk will show itself with radial velocities higher than that of thick disk by similar amount as seen in this direction. To investigate whether an inadequate model of thin disk stars contributes to the mismatch, one may consider comparing R313 with the correspondingly low Galactic latitude WGN field near $RA \sim 133^\circ$ ($l = 228^\circ, b = +27^\circ$). We found, especially by comparing the metallicity distributions in these two directions, that there is no significant contribution from a thin disk population. By looking at the number of stars in each field as given by the Besançon Model of the Galaxy (Robin et al. 2003) on applying the WGN colour-magnitude cuts, we verify that the number of thin disk stars that pass the selection function is minimal, the contamination being close to 0 in most of the high latitude fields and between 5 and 15% in all the lowest latitude fields, as shown in Figure 12. The thin disk kin-

Table 3. Kinematic parameters adopted and determined in the Galactic model

Parameter	Value fixed (km/s)	Value determined (km/s)	Reference
Halo			
V_R, V_ϕ, V_Z	0, 0, 0		assumed
σ_{V_R}	150 ± 2		Carollo et al. (2010)
σ_{V_ϕ}	95 ± 2		Carollo et al. (2010)
σ_{V_Z}	85 ± 1		Carollo et al. (2010)
Thick Disk			
V_R, V_Z	0, 0		assumed
V_ϕ, σ_{V_ϕ}		$172 \pm 2, 49 \pm 2$	this study
σ_{V_R}		51 ± 3	this study
σ_{V_Z}		40 ± 3	this study

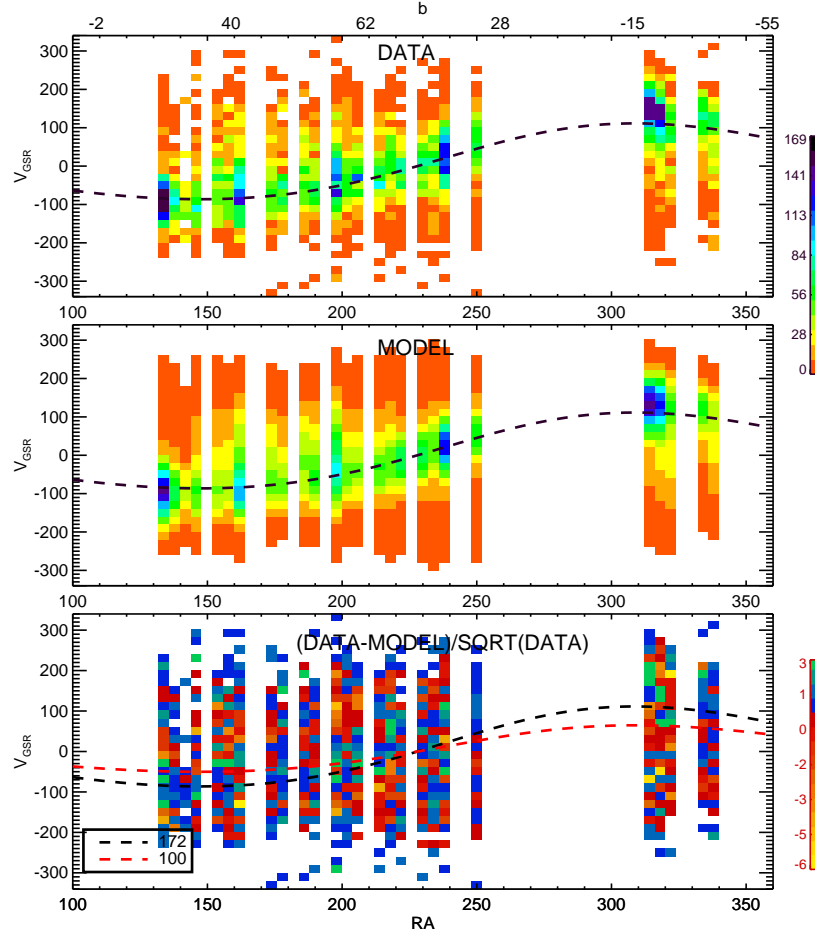


Figure 17. Galactocentric velocity vs RA is plotted for the weighted data (top panel) and for the model with our best fit thick disk rotational parameters of $V_\phi, \sigma_{V_\phi} = 172, 49 \text{ km/s}$ and $\sigma_{V_R}, \sigma_{V_Z} = 51, 40 \text{ km/s}$ (middle panel). For these two panels, colours indicate the number of stars in each bin, as indicated. The dashed lines correspond to a rotational velocity of 172 km/s, the determined best fit mean, at 2 kpc. Both data and model plots have been normalised to have 1000 stars in each field in order to bring out features more clearly. All the velocity parameters of the halo are fixed in the model. (see Table 3). The relative normalisation between thick disk and halo for each field is allowed to be a free parameter. Lower panel: this shows the significance of the difference between the model and the data. In this panel, blue to green denotes positive deviation ranging from 0 to $+3\sigma$ while red to orange denotes 0 to -6σ . The dashed lines in the lower panel correspond to a rotational velocity of 172 km/s and 100 km/s at a distance of 2 kpc, and are illustrative. Galactic latitude is also indicated at the top of upper panel.

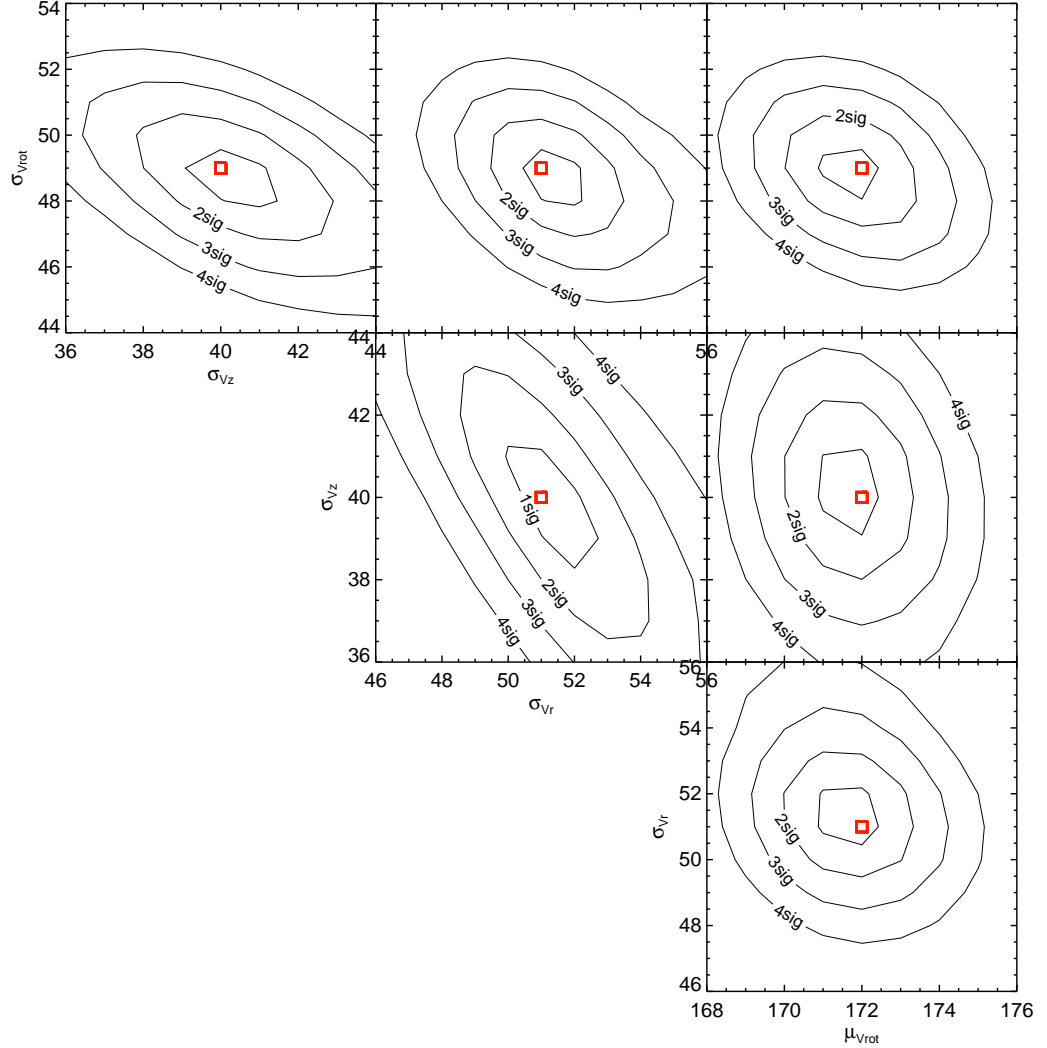


Figure 18. The likelihood contours of the four thick disk kinematic parameters determined in the maximum likelihood fitting of the model - $V_\phi, \sigma_\phi, \sigma_R, \sigma_Z$. The red box in each case marks the value for which the likelihood is maximised.

matic signal, if present, may be unidentifiable towards the Galactic centre, near fields $RA \sim 249^\circ$, but $RA \sim 133^\circ$ being similarly inclined to the centre-anti-centre line as $RA \sim 313^\circ$, we would expect the thin disk stars to equally show themselves in the line of sight velocity distributions in these fields as well, but this is not the case. The data match our kinematic model well near $RA \sim 133^\circ$. Hence we conclude that a misrepresentation of the high-latitude symmetric thin disk cannot be the cause of the excess numbers of stars with high line of sight velocities. For similar reasons, the fact that we may have ignored any vertical velocity gradient in the kinematic model for the thick disk is an unlikely cause of the mismatch.

Might incorrect interstellar extinction be at fault? If one underestimates the extinction one overestimates the distance, which can make stars in this region appear to be moving faster. The estimated distance of stars in R313 is on average between 2 to 3 kpc. However, even a 25% distance error increases the V_{GSR} at $RA \sim 313^\circ$ only by 5 km/s for a rotational velocity of 180 km/s. Therefore, overestimated

distances due to incorrect extinction cannot produce as significant a shift in V_{GSR} as is being observed here. This would also not explain the excess star counts discussed in the next section.

The above checks confirm that the velocity mismatch seen in region R313 is real and due to some substructure.

4.4 Modelling number counts - the thick disk scale length

We look at *how many* stars in the R313 fields contribute to the velocity mismatch. For this, we first assume that the substructure is disk-like with similar V_R and V_Z distributions as the thick disk, but a higher mean V_ϕ . We fix the halo kinematics as before and fix the thick disk kinematics to the values determined from the global fit in Section 4.2. We isolate four WGN fields that cover region R313 and fit for V_ϕ and σ_ϕ of the substructure. We obtained a maximum likelihood fit of $V_\phi, \sigma_\phi = 206, 36$ km/s. As shown in Figure 19 the substructure has a 35% and 30% contribution to the

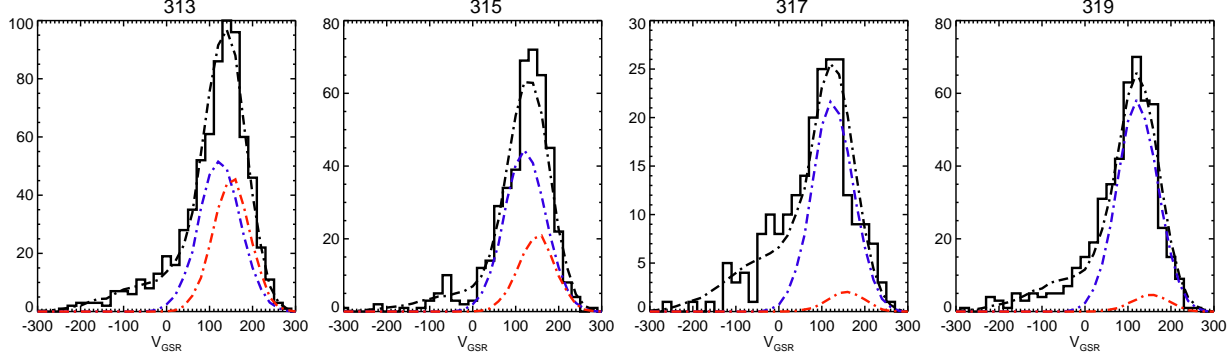


Figure 19. The panels show line of sight velocity for four fields near R313 where the mismatch in velocities between data and model is apparent. Data in these fields are simultaneously fit by three components - thick disk, halo and a third component representing the overdensity. Halo kinematics are held fixed as before (Table 3). Thick disk kinematics are adopted from the fit result in Section 4.2 i.e. $V_\phi, \sigma_{V_\phi}, \sigma_{V_R}, \sigma_{V_Z} = 172, 49, 51, 40$ km/s with mean V_R, V_Z fixed to zero. The overdensity is assumed to be thick disk like, albeit with a different rotation velocity. All parameters for the overdensity are fixed to thick disk values, except V_ϕ, σ_{V_ϕ} which are fit by maximum likelihood. The best fit value obtained was 206,36 km/s. The histograms show the unweighted data, the blue curve show the thick disk model, red curve shows the overdensity model and the black curve shows the total model in each case. The RA of the field is indicated above each panel. The contribution of this extra component is as high as 35% and 30% in the left two panels while it drops to 5% in the last two.

fields centred on RA 313° and 315° respectively while the contribution falls sharply to 5% in the fields centred on RA 317° and 319° . We should expect these stars to show up as an excess in number count distributions of the thick disk.

We therefore go on to analyse the number of stars per field present in the SDSS DR7 data adopting the same colour-magnitude cuts as the WGN selection function, and compare this to the number count predictions given by the Besançon Model of the Galaxy. This comparison is shown in Figure 20, where significant differences between the model and the data are evident in the RA ranges which correspond to the lowest Galactic latitudes (RA $\sim 133^\circ$ and RA $\sim 313^\circ$). The default extinction in the Besançon model is smaller than in SDSS data, so we also show model predictions adopting the SDSS DR7 mean extinction in each field, confirming a real difference between model and data.

In order to understand the reasons for this difference between model and data, we describe here a simple toy-model analysis. We generated the star count density distribution of the thick disk and halo using respectively a double exponential disk parametrised by scale height h_Z and scale length h_R to describe the density distribution of the thick disk and a flattened power-law with flattening $q = 0.6$ and index $\alpha = 2.3$ to describe the halo (Deason, Belokurov & Evans 2011), with the number of halo to thick disk stars fixed within the Galaxy. In Figure 21 we show the number distribution generated by this model for the WGN fields and selection function.

In the top panel of Figure 21 h_Z is kept fixed at 0.9 kpc and h_R varied from 2 to 8 kpc, while in the middle panel h_R is fixed at 4.0 kpc while h_Z is varied from 0.7 to 1.3 kpc. From the plots, we can see that the number counts at lower Galactic latitudes are the most sensitive to thick disk structural parameters - as the thick disk scale length is increased (or, with less effect, the scale height is decreased), the number of stars near RA $\sim 135^\circ$ and RA $\sim 315^\circ$ increases. The data are mostly sensitive to the thick disk radial scale length and a sufficient range of fields has been targeted to provide use-

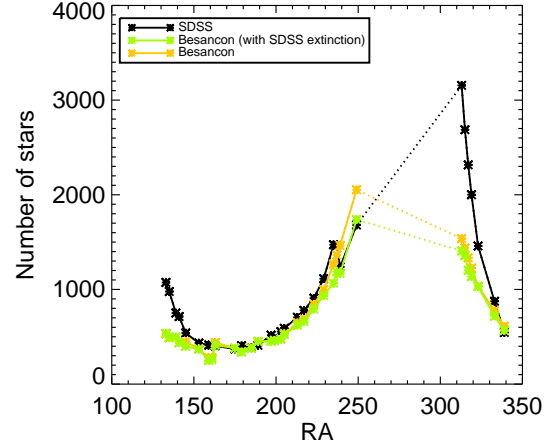


Figure 20. The surface number density distribution of stars per WGN field is compared between SDSS DR7 and the Besançon Model of the Galaxy for a magnitude range of $16 \leq g \leq 17.5$ and same colour cuts as the WGN selection function. black : SDSS DR7 data ; orange : Besançon Model values ; green : Besançon model number counts corrected with the corresponding extinction for each field from SDSS DR7. SDSS data shows an excess of stars in comparison to the Besançon model in two regions - RA less than 140° and RA in the range 313° to 330° , which figure 21 shows is the region sensitive to thick disk structural parameters.

ful constraints on those structural parameters. This analysis thus illustrates the utility of the range of fields selected for observation by WGN as a test of thick disk structural parameters.

We define two figures of merit, Ratio1, being the ratio of the number of stars per square degree selected by the WGN criteria in the field at RA $= 313^\circ$ to the corresponding number for the field at RA $= 249^\circ$; and Ratio2, the corresponding number comparing the star counts in the field at RA $= 133^\circ$ to those in the field at RA $= 249^\circ$. These figures

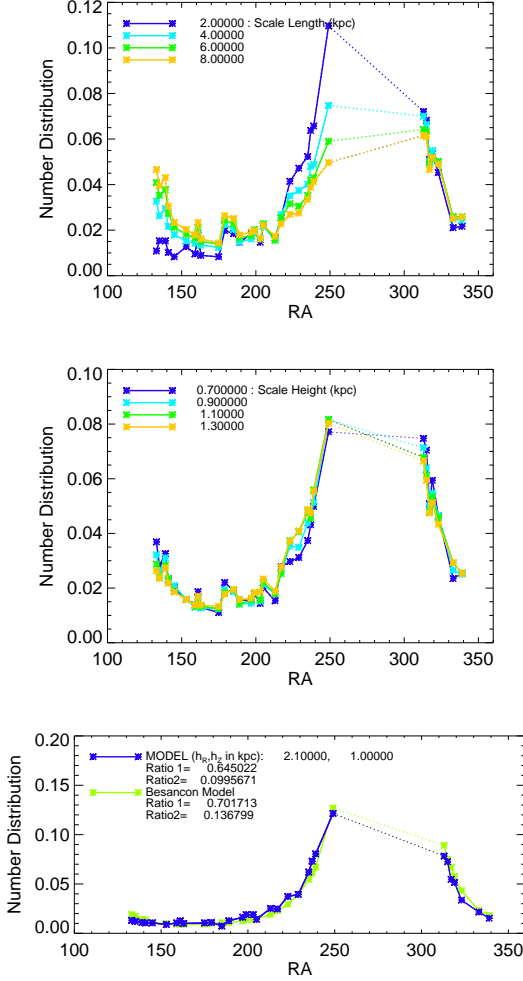


Figure 21. A simple illustration of the sensitivity of star counts in the WGN fields to the structural parameters of the thick disk. The figure shows number count distributions produced by a simple density model for thick disk-halo : a double exponential disk parametrised by scale height h_z and scale length h_R for the thick disk and a flattened power-law with flattening $q = 0.6$ and index $\alpha = 2.3$ for the halo. Distributions are obtained for the WGN lines of sight for stars in a 6 kpc region centred on the Sun. The global ratio of halo to thick disk stars in the Galaxy is held fixed. Top: h_z fixed at 0.9 kpc. h_R varied from 2 to 8 kpc in steps of 2 kpc. Middle: h_R fixed at 4 kpc. h_z varied from 0.7 to 1.3 kpc in steps of 0.2 kpc. We can see that increasing h_R or decreasing h_z significantly changes the number counts near $RA \sim 135^\circ$ and $RA \sim 315^\circ$, which correspond to the lowest Galactic latitudes probed. Bottom: Comparison of the simple parametric star count galaxy model with star count distributions in the WGN fields predicted by the Besançon model. The values of the two figures of merit defined in the text, Ratio1 and Ratio2, are given for the distributions for quantitative comparison. The model with $h_R, h_z = 2.0, 0.8$ kpc (blue) reproduces the number distribution of the Besançon model (green) adequately, showing these are equivalent exponential scale lengths to the model for present comparative purposes.

of merit quantify how the change in the thick disk structural parameters h_R, h_z affect the shape of the star counts distribution as a function line of sight. The star count distributions produced by the Besançon model has Ratio1=0.66 and Ratio2=0.20 while the observed distribution from SDSS data has Ratio1=1.69 and Ratio2=0.37. This quantifies the discrepancy between data and model evident in Figure 20.

By experiment we see that $(h_R, h_z) = 2.1, 1.0$ kpc reproduces the Besançon number distribution well (shown in bottom panel of Figure 21). That is, the Besançon model description of the thick disk, for the observational parameters of relevance here, may be described as a double exponential with $(h_R, h_z) = 2.1, 1.0$ kpc. This is consistent with values quoted in Robin et al. (2003) as used in the model for the thick disk density profile which is a modified exponential having scale length of 2.5 ± 0.5 kpc, and scale height of 0.8 ± 0.5 kpc. As shown in Figure 20, however, that model substantially and systematically under-predicts the observed SDSS star counts. Increasing the radial thick disk scale length to the value $h_R = 4.1$ kpc, as shown in Figure 22, makes the shape of the number distribution consistent with SDSS data. This number is in agreement with the value obtained by Juric et al. (2008) who analyse M dwarfs in the solar neighbourhood (at distances less than 2 kpc) from SDSS data to estimate a scale length of 3.6 kpc for the thick disk. While most previous works which estimate the scale length using star count analysis obtain scale length values between 3.5 and 4.5 kpc which is consistent with our analysis here, those works which have employed population separation based on a kinematic or chemical selection, such as Bensby et al. (2011) and Cheng et al. (2012b), estimate a much lower scale length of around 2kpc. Understanding this difference will no doubt significantly improve definition of the astrophysical nature of the thick disk.

While an increased h_R reproduces the observed value of Ratio2, there is still a large disagreement in Ratio1 (compare black line (data) and blue line (model) in Figure 22). Subtracting from the data the contribution of the high velocity substructure determined from Figure 19 (red line), we see that the match improves for Ratio1 too.

Thus, from this simple toy-model analysis we deduce a value of ~ 4.0 kpc for the thick disk scale length. We find that a smooth double-exponential is, however, not a complete description of the data and a substantial overdensity, compared to this model, is apparent in the star counts, localised near $RA \sim 313^\circ$. This overdensity matches the fraction of stars contributed by the high-velocity sub-structure identified in the previous section.

In the next section, we analyse and characterise the stars in this sub-structure.

4.5 Characterising the stars in the thick disk substructure

In Figure 19 we have already shown that the most significant contribution of stars which have high velocity compared to the model fit is restricted to just two fields in WGN (spanning around 4° in RA), beyond which the uniform thick disk model well reproduces the line of sight velocity distributions.

Figure 23 shows the colour-magnitude diagram of these two fields in the region R313 where the contribution of the high velocity stars is most significant. We see that both the

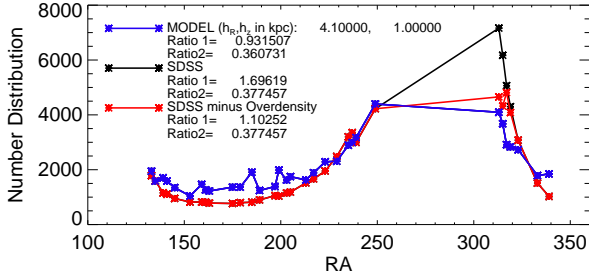


Figure 22. Comparison of SDSS photometric star count data in the WGN fields and the simple star count model described in the text. In the region $RA \leq 250^\circ$ the star count data (black) and the simple model (blue) are in tolerable agreement. This indicates a photometric thick disk model with $h_R, h_Z = 4.1, 1.0$ kpc is an adequate description of the Galaxy. For $RA \geq 300^\circ$ the SDSS star count data (black) are significantly in excess of the model (blue), indicating an additional structure in the Galaxy. The red curve illustrates the SDSS count data after subtraction of a model for the excess counts described in the text and in Figure 19. This “thick disk plus over-density” model is an adequate description of the underlying “normal” thick disk population.

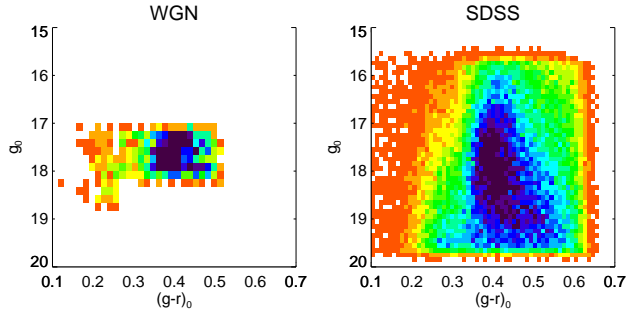


Figure 23. Left : Colour-magnitude diagrams from WGN data for two fields, covering the region $312^\circ < RA < 316^\circ$ and $-1^\circ < Dec < 1^\circ$. Binsize for this CMD is $\Delta g - r, \Delta g = 0.015, 0.15$. Right : CMD from SDSS DR7 data for a larger region around the same fields covering $310^\circ < RA < 318^\circ$ and $-3^\circ < Dec < 3^\circ$. Binsize for this CMD is $\Delta g - r, \Delta g = 0.01, 0.1$. The stars from the overdensity overlap with the thick disk turn off stars and are indistinguishable from thick disk. The colours denote low to high density from red to blue

WGN and SDSS DR7 CMD look thick disk-like with the high-velocity stars overlapping with thick disk stars. No special feature in the CMD or extra turn-off is apparent. The substructure has a spread in apparent magnitudes as indicated by Figure 24, but is preferentially seen at brighter magnitudes, being most prominent at magnitudes brighter than $g \sim 17.3$. The null hypothesis that the two curves (black and red) in Figure 24 are drawn from the same distribution is rejected at the 5 percent level based on the Kolmogorov Smirnov Test. The same comparison was done for $RA \sim 133$ and the null hypothesis was accepted.

Figure 24 also reveals that the substructure has metallicity somewhat below the thick disk, with mean metallicity around -1.0 dex (black line).

Is it reasonable for us to assume the excess stars are

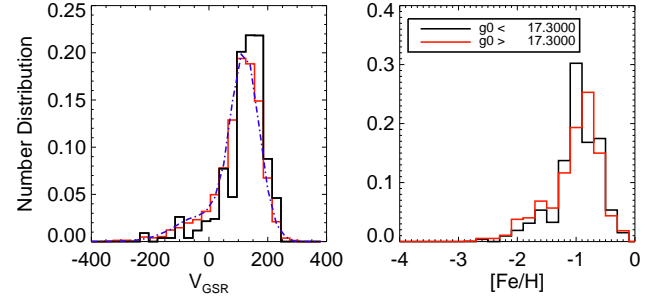


Figure 24. Unweighted line of sight velocity histograms are shown for all stars in three fields from WGN covering $312^\circ < RA < 318^\circ$. The sample is divided into brighter and fainter than $g_0 = 17.3$. The left panel shows the line of sight velocities (histograms) with the blue dot-dash curve showing the expected model distribution. The right panel shows the metallicity distributions. The excess stars are most apparent with velocities somewhat higher than that of the thick disk, with metallicity near $[Fe/H] = -1$, and at brighter magnitudes.

in thick disk-like orbits? We looked at the V_R, V_ϕ, V_Z distribution of stars from this line of sight by cross matching the WGN data with proper motions from Stripe 82 based on position, being aware from our analysis above (Figure 16) that such comparisons are indicative rather than conclusive. We used new high-precision values of SDSS star proper motions re-calibrated by Koposov et al. (2013) using background galaxies. 613 matches were obtained. Stars with proper motion errors greater than 30mas/yr were removed. Figure 25 shows the velocity distributions for the region of interest ($312^\circ < RA < 317^\circ$) compared to distributions from nearby fields with no excess ($RA > 317^\circ$). The V_ϕ and V_Z distributions of the two sets of fields are indistinguishable. This is consistent with the excess stars being in thick disk-like orbits. Whereas, the mean V_R of the fields in R13 is offset towards positive values.

4.6 Complementary and pre-discovery studies

An independent source of kinematics in the region of interest comes from other SDSS studies, the SDSS spectra themselves. The SDSS DR7 spectra, selected applying the WGN selection function, hint at a cold high velocity structure which is spatially and kinematically consistent with R13. Figure 26 shows line of sight velocities from SDSS DR7 for a region $312^\circ < RA < 326^\circ$ and $-10^\circ < Dec < 10^\circ$. Each panel is a 4° block in RA, the mid value of RA being shown at the top of each panel. The colours represent low to high density from red to blue while the dashed line shows the position of thick disk rotation (i.e $V_\phi = 172$ km/s) at a distance of 2 kpc for each direction and serves as a reference. If velocities are consistent with being thick disk, we would expect the peak in density in each bin of declination to coincide with the dashed line. We can see that this is the case in most bins, apart from an excess of stars at relatively high V_{GSR} velocities (immediately to the right of the dashed line) in the first two panels at $Dec \sim 0^\circ$. This is consistent with the high velocity stars seen in the WGN data. For clarity, recall that these stars have observed radial velocity V_{helio} near zero (cf fig 3). Any selection effects in

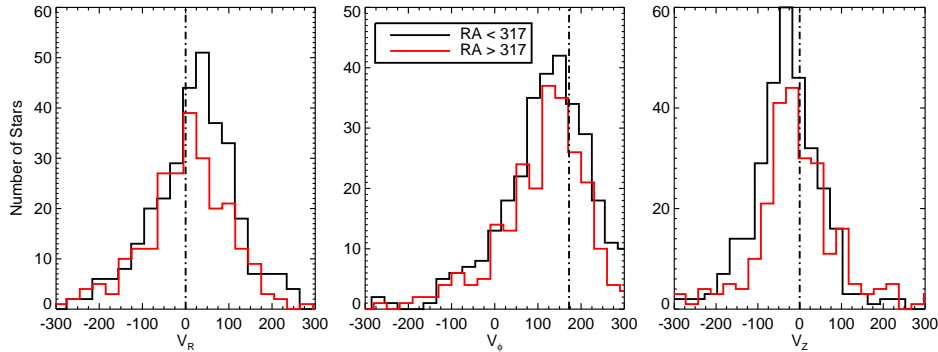


Figure 25. Galactocentric velocity distributions for the region with the star-count excess, R313 (black histogram), is compared to distributions from fields with $RA > 317^\circ$ which do not show a star count excess (red). The V_ϕ and V_z distributions are comparable, indicating a thick-disk-like velocity pattern, while the mean V_R of the fields in R313 is offset towards positive values.

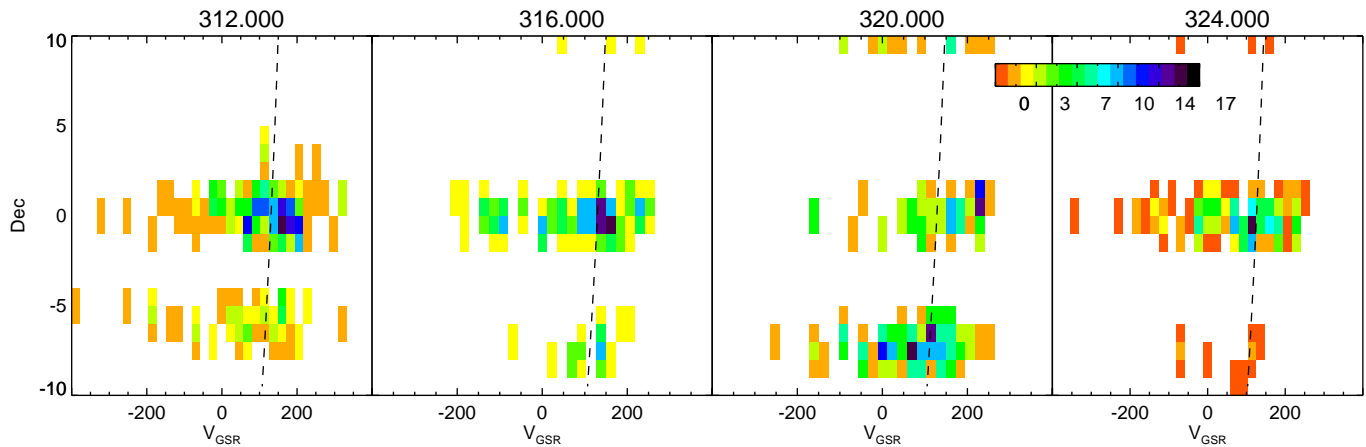


Figure 26. Radial velocities from SDSS DR7 spectra for a region $312^\circ < RA < 326^\circ$ and $-10^\circ < Dec < 10^\circ$, applying the WGN selection function. Each panel is a 4° block in RA, the mid value of RA being shown at the top of each panel. The colours represent low to high density from red to blue. The dashed line shows the position of thick disk rotation (i.e. $V_\phi=172$ km/s) at a distance of 2 kpc for each direction. We can see that there is an excess of stars at high V_{GSR} , that is here, close to zero V_{helio} velocities (immediately to the right of the dashed line) in the first two panels, consistent with the excess stars seen in the WGN data.

SDSS spectroscopy are unlikely to vary enough from field to field, within the tight cuts of the WGN selection function, to change this result.

The overdensity observed by us is in a direction of the sky that is extremely busy, with previously identified sub-structures such as the Hercules Thick Disk Overdensity at 1-2 kpc, Hercules Aquila Cloud at 10-20kpc and more recent sub-structure observed in RR Lyrae stars in Stripe 82 at 10-25kpc.

The Hercules Thick Disk Overdensity, first identified and studied in detail by Larsen & Humphreys (1996), and further investigated in subsequent papers (Larsen et al. (2010), Larsen et al. (2011), Humphreys et al. (2011)) thereafter, is an excess of faint blue stars in the region $\ell = 20^\circ - 55^\circ$ and $|b| = 20^\circ - 45^\circ$, thus overlapping with R313. These stars were estimated to have distances between 1-2 kpc from the sun, consistent with distances estimated by our method for our stars. Humphreys et al. (2011) additionally also provide velocity measurements for their fields. They found that stars in Quadrant I (where the excess stars were found) had a V_{LSR} of -28.6 ± 1.6 km/s above the plane

and a V_{LSR} of -35.6 ± 2.0 km/s below the plane. They also state that going beyond 4 kpc along the line of sight, where the overdensity coincides with the density contours of the Galactic bar, the rotational rates become larger than standard thick disk rotation. These kinematic parameters are in agreement with those we find here, though our sample here is very much more spatially concentrated than is that of Humphreys et al. (2011).

The Hercules Aquila Cloud (Belokurov et al. 2007) is thought to be a large structure further out in this same direction, centred on $l \sim 40^\circ$ and extending both above and below the plane up to $b \sim 50^\circ$. The cloud was estimated to be more metal rich than -2.2 dex and have distances in the range of 10-20kpc. Their paper quotes a corresponding kinematic signature of $V_{GSR} = 180$ km/s associated with this cloud which matches the kinematic signal we find in the WGN data.

We also looked at the density of RR Lyrae stars in Stripe 82 (Sesar et al. 2010), and towards the Hercules-Aquila density enhancement. In Figure 11 of Sesar et al. (2010), the overdensity marked B is centred on similar direc-

tions as our overdensity, but extends between 5 and 25kpc. Cross-matching these stars with Sloan spectroscopy resulted in a handful of matches. While these stars showed a peak in $[\text{Fe}/\text{H}]$ near -1.5dex, we did not find a coherent velocity for stars in this structure.

Given there are at least two known overdensities in this direction at distances beyond 10kpc, we investigated the possibility of the stars in our overdensity in fact being at distances beyond 10kpc, but being assigned grossly underestimated distances by our by our analysis techniques. Looking at the predictions from the Besançon model, we find that few sub-giants at large distances (further than 10kpc) pass through the WGN selection function and such stars fall in the very red, faint end of the WGN selection box. Our distance determination will indeed grossly underestimate the distances to these stars, putting them at 2-4 kpc. But this would require that all of the stars in the overdensity be clearly concentrated in colour-magnitude space at the faint-red end. As seen from Figure 23 this is not the case. The overdensity stars instead look very thick-disk like.

5 CONCLUSIONS

We analyse the WGN medium resolution AAOmega spectroscopic survey of some 10,000 stars, selected using SDSS photometry to be main sequence turn-off stars in the thick disk-halo interface. The goal has been to investigate large-scale and small-scale kinematic, chemical and spatial properties of these two old stellar populations, and additionally also investigate the region of transition/overlap between these two populations.

Preparatory to the analysis, we developed a weighting method in colour-magnitude space for completeness correction. Applying this correction, we obtained a completeness-corrected representation of the parent stellar population selected by the WGN selection function, thus preparing the data for analysis. Robust distance estimates were obtained by isochrone fitting, using either or both of SDSS *gri* and UKIDSS JHK photometry, for the stars, providing distances with a systematic uncertainty of less than 10%.

We demonstrated how it is convenient to model the data in observable space directly. Propagated errors in derived parameters, especially those in V_R , V_ϕ , V_z due to proper motions, can be dominant, and hence deconvolution can degrade the most accurate data, here radial velocities and $[\text{Fe}/\text{H}]$ values, from any analysis. Hence, we analysed the kinematics of the thick disk using only observable line of sight velocities, adopting the technique from Sirko et al. (2004) and limiting the use of derived parameters to that of distance alone. In this study, we obtain a global description of the thick disk kinematics to demonstrate the scope of the data and the efficiency of the technique. The best fit thick disk kinematic parameters are determined to be $V_\phi=172$ km/s and $\sigma(\phi, r, z) = (49, 51, 40)$ km/s which agrees reasonably well with values from previous studies.

By comparing this global model description with the data, we identify a region near $\text{RA} \sim 313^\circ$ which has higher line of sight V_{GSR} velocities than expected for the thick disk in this region. The same region is found also to have a local overdensity of stars in comparison to that expected for thick disk density models. The stars in the overdensity

have a turn-off CMD similar to that of the thick disk and metallicities ~ -1 dex, similar to, but slightly more metal poor than, the thick disk (Carollo et al. 2010). The stars in the excess are thus as old as are those of the thick disk. The overdensity decreases rapidly over a 4° increase in RA from 312° . Its further extent is poorly determined as yet.

This overdensity spatially may be associated in some way with the Hercules thick disk overdensity. Line of sight velocity measurements from Humphreys et al. (2011) match with the overdensity found in our WGN data, but they infer lower rotational velocities than thick disk for the stars in the overdensity while given our distance range we infer the opposite. We should have also expected the velocity signature to continue till at least RA of 320° if associated with the Hercules thick disk overdensity which is a large structure. This line of sight is towards the Hercules-Aquila halo cloud and a small spatial-scale overdensity in the RR Lyrae distribution. Obtaining reliable velocity estimates for these structures would be illuminating.

We have shown that the method of modelling in observable space is very powerful not only to obtain a global description of the Galactic stellar populations, but also to identify and pick out substructure. We will extend this method in future work, to include scientifically important questions of spatial gradients in structure, kinematics and metallicity in the thick disk.

ACKNOWLEDGMENTS

AJ thanks The Boustany Foundation and Isaac Newton Trust for the award of scholarships. VB acknowledges financial support from the Royal Society. RFGW acknowledges support from National Science Foundation grants AST-0908326 and CDI-1124403, and thanks the Aspen Center for Physics, supported by the National Science Foundation grant PHY-1066293, for hospitality. .

REFERENCES

- Abazajian K.N. et. al., 2009, ApJS, 182, 543
- An D. et al., 2008, ApJS, 179, 326
- An D. et al., 2009, ApJ, 700, 523
- Anthony-Twarog, B.J., Tanner, D., Cracraft, M., Twarog, B.A., 2006, AJ, 131, 461
- Bahcall, J. et al., 1985, ApJ, 299, 616
- Beers T.C. et al., 1999, AJ, 117, 981
- Belokurov V., et al., 2007, ApJ, 657, L89
- Bensby T., Feltzing S., 2012a, EPJWC, 19, 4001
- Bensby T., Feltzing S., 2012b, 2012,ASPC,458,201B
- Bensby T., Alves-Brito A., Oey M. S., Yong D., Meléndez J., 2011, ApJ, 735, L46
- Bensby T., Alves-Brito A., Oey M. S., Yong D., Meléndez J., 2012, ASPC,458,171B
- Bond N.A. et al., 2010, ApJ, 716, 1
- Bovy J., Rix H., Hogg D.W., 2012,ApJ, 751, 131
- Carney B.W., 1979, ApJ, 233, 211C
- Carollo D. et al., 2010, ApJ, 712, 692
- Cheng J. Y. et al., 2012a, ApJ, 746, 149
- Cheng J. Y. et al., 2012b, ApJ, 752, 51
- Chiba M., Beers T. C. 2000, AJ, 119, 2843

- Deason A. J., Belokurov V., Evans N. W., 2011, MNRAS, 416, 2903
- Dotter A., Chaboyer B., Jevremovic D., Kostov V., Baron E., Ferguson J.W., 2008, ApJS, 178, 89
- Eggen O. J., Lynden-Bell D., Sandage A. R., 1962, ApJ, 136, 748
- Fenkart, R.P. 1989 A&AS 78 217
- Fuhrmann K., Chini R., Hoffmeister V. H., Bernkopf J., 2012, MNRAS, 420, 1423
- Fuhrmann K., 2011, MNRAS, 414, 2893
- Fuhrmann K., 2008, MNRAS, 384, 173
- Fuhrmann K., 2004, AN, 325, 3
- Gilmore G., Wyse R.F.G., Jones, J.B., 1995, AJ, 109, 1095
- Gilmore G., Wyse R.F.G., Kuijken K., 1989, ARAA, 27, 555
- Girardi L., Grebel E.K., Odenkirchen M., Chiosi C., 2004, A&A, 422, 205
- Hewett P. C., Warren S. J., Leggett S. K., Hodgkin S. T., 2006, MNRAS, 367, 454
- Humphreys R.M., Beers T.C., Cabanela J. E., Grammer S., Davidson K., Lee Y.S., Larsen J.A., 2011, AJ, 141, 131
- Ivezic Z. et al., 2008, ApJ, 684, 287
- Johnson D.R.H., Soderblom D.R., 1987, AJ, 93, 864
- Juric M. et al., 2008, ApJ, 673, 864
- Kalirai J.S., 2012, Nature, 486, 90
- Kerr F. J., Lynden-Bell D., 1986, MNRAS, 221, 1023
- Koposov S. et al., 2012 in preparation
- Kordopatis G. et al., 2011, A&A, 535A, 107
- Kraft R.P., Ivans I.I., 2003, PASP, 115, 143
- Larsen J.A., Humphreys R.M., 1996, ApJ, 468L, 99
- Larsen J.A., Cabanela J.E., Humphreys R.M., Haviland A.P., 2010, AJ, 139, 348
- Larsen J. A., Cabanela J. E., Humphreys R. M., 2011, AJ, 141, 130
- Lee Y. S., et al., 2011, ApJ, 738, 187
- Liu C., van de Ven G., 2012, EPJWC, 19, 4007
- Reddy B. E., 2007, IAUS, 241, 209
- Reddy B. E., 2010, IAUS, 265, 289
- Reddy B. E., Lambert D. L., 2008, MNRAS, 391, 95
- Reddy B. E., Lambert D. L., Allende Prieto C., 2006, MNRAS, 367, 1329
- Reddy B. E., Lambert D. L., Allende Prieto C., 2008, MRU,conf, 69R
- Robin A.C., Reyle C., Derriere S., Picaud S., 2003, A&A, 409, 523
- Ruchti G. R., et al., 2011, ApJ, 737, 9
- Sandage A. R., Eggen O. J., 1959, MNRAS, 119, 278
- Schönrich R., Binney J., Dehnen W., 2010, MNRAS, 403, 1829
- Schlesinger K. J., et al., 2012 ApJ, 761, 160S
- Sesar, B. et al., 2010, ApJ, 708, 717
- Sills, A., Pinsonneault, M. H., Terndrup, D. M. 2000, ApJ, 534, 335
- Sirko E. et al., 2004, AJ, 127, 914
- Smith M. C., Whiteoak S.H., Evans N. W., 2012, ApJ, 746, 181
- Smith M.C. et al., 2009, MNRAS, 399, 1223
- Wallerstein G., 1962, ApJS, 6, 407
- Wolf C. et al., 2004, A&A, 421, 913
- Wyse R.F.G., Gilmore G., Norris J.E., 2006, BAAS, Vol. 38, p.1149
- Wyse R.F.G., Gilmore G., Norris J.E., 2013 in preparation
- Yoshii, Y., chapter 8 in vol 5 of Planets, Stars and Stellar Systems, ed G Gilmore (Springer, in press) 2013